Light affects the prefrontal cortex via intrinsically photosensitive retinal ganglion cells

Lorenzo Lazzerini-Ospri[1], Jesse J. Zhan[1,2], Michael B. Thomsen[1,2], Hui Wang[2], Fany Messanvi[2], Johann du Hoffmann[2], Kevin Cravedi[2], Ruchi Komal[2], Yogita Chudasama[2*], Haiqing Zhao[1*], Samer Hattar[2*]

[1]Johns Hopkins University, Department of Biology, Baltimore MD 21218, USA

[2]National Institutes of Health, National Institute of Mental Health, Bethesda MD 20892, USA

*co-correspondence samer.hattar@nih.gov, hzhao@jhu.edu, yogita.chudasama@nih.gov

Editorial correspondence:

Samer Hattar, PhD
Section on Light and Circadian Rhythms
National Institute of Mental Health (NIMH)
National Institutes of Health (NIH)
Building 35A, Room 2E-450
Bethesda, MD 20892, USA
Phone: +1-301-435-1887
Email: samer.hattar@nih.gov

Highlights

1- ipRGCs regulate ventromedial prefrontal cortex (vmPFC) activity and function
2- ipRGCs mediate these effects through light, independent of circadian and mood alterations
3- Behavioral assays implicate ipRGCs in the regulation of emotions by the vmPFC
4- ipRGCs mediate these effects through a retina-corticolimbic pathway not involving the visual cortex

Abstract

The ventromedial prefrontal cortex (vmPFC) is a part of the limbic system engaged in the regulation of social, emotional and cognitive states, which are characteristically impaired in disorders of the brain such as schizophrenia and depression. Here, we show that intrinsically photosensitive retinal ganglion cells (ipRGCs) modulate, through light, the integrity, activity and function of the vmPFC. This regulatory role, which is independent of circadian and mood alterations, is mediated by an ipRGC-thalamic-corticolimbic pathway. Lack of ipRGC signaling in mice causes dendritic degeneration, dysregulation of genes involved in synaptic plasticity, and depressed neuronal activity in the vmPFC. These alterations primarily undermine the ability of the vmPFC to regulate emotions. Our discovery provides a potential light-dependent mechanism for certain PFC-centric disorders in humans.

Introduction

In mammals, non-image-forming visual functions such as circadian photoentrainment, pupillary light response and mood regulation by light exposure are dependent on a subpopulation of retinal ganglion cells (RGCs) made intrinsically photosensitive (thus ipRGCs) by their expression of the photopigment melanopsin (Opn4) (Provencio & Warthen, 2012; Hattar et al, 2002; Berson et al, 2002; Provencio et al, 2000; Güler et al, 2008). These ipRGCs are diverse, comprising at least six subtypes (M1-6) (Ecker et al., 2010; Quattrochi et al., 2019; Schmidt et al., 2014) distinguished by size, dendritic stratification, and electrophysiological properties. Their central projections also differ, reflecting the diverse biological functions that ipRGCs regulate (Lazzerini Ospri et al., 2017). Among the brain regions ipRGCs innervate is the perihabenula (PHb) (Fernandez, Fogerson, Lazzerini Ospri et al., 2018), a nucleus of the dorsal thalamus that mediates the direct effects of light on mood (Fernandez et al., 2018, LeGates et al., 2012, Fernandez, Fogerson, Lazzerini Ospri et al., 2018). The PHb densely innervates the ventromedial subdivision of the prefrontal cortex (PFC) (Fernandez, Fogerson, Lazzerini Ospri et al., 2018), and thus relays retinal input directly to this region.

The prefrontal cortex organizes goal-directed behaviors, its main domains being planning, decision making, executive attention and emotional regulation (Fuster, 2001, Franklin and Chudasama, 2012). A distinction is drawn between the dorsolateral PFC, implicated in purely cognitive functions, and a paralimbic PFC, comprising the orbital and ventromedial areas, involved in evaluating the emotional significance of events and regulating emotions for the purposes of goal-directed behavior (Fuster, 2001, Morgan et al., 1993, Franklin and Chudasama, 2012). In mice, the ventromedial prefrontal cortex (vmPFC) encompasses the prelimbic and infralimbic cortex (Franklin and Chudasama, 2012). It is part of a broader network interconnecting limbic and associative areas such as the

basomedial amygdala and the ventral striatum, the hypothalamus and the brainstem (Adhikari et al., 2015; Vertes, 2004), and thereby contributes to a wide range of functions. Lesion studies in mice implicate the vmPFC in social cognition (Bicks et al., 2015), the regulation of fear and anxiety (Sotres-Bayon and Quirk, 2010), and the cognitive control of actions (Latif-hernandez et al., 2016). These behavioral deficits are a core feature of many clinical populations including those suffering from depression and schizophrenia, who are known to have a compromised vmPFC (Chudasama and Robbins 2006, Bicks et al., 2015). Despite its clinical importance, and the fact that it is interconnected with many areas directly or indirectly receiving photic input, to date, there is no indication that this region may be affected by light exposure, an important environmental variable. Here we show that light exposure regulates the integrity, activity, and function of the vmPFC through an ipRGC-thalamic-prefrontal pathway that is independent of the visual cortex.

Results

Dark-reared mice or mice lacking ipRGC exhibit reduced apical dendritic arborization in the vmPFC

Within the vmPFC, PHb innervation encompasses layers I and III/IV of the infralimbic and prelimbic cortex. Previous studies showed that chronic exposure of animals to constant darkness (known as a dark-dark or DD) delays the normal development of the primary visual cortex (Gianfranceschi, et al., 2003, Izquierdo et al., 2006, Perez-Cruz et al., 2009). To address whether light exposure affects the vmPFC, we prepared and analyzed Golgi-stained coronal sections along the anterior-posterior extent of the infralimbic and prelimbic cortex. One group of control mice were maintained on a standard 12-hour light – 12-hour dark cycle (12:12 LD), and another group of experimental mice were kept in DD prior to birth and up to 4 months after birth. We then reconstructed the apical dendritic arbors of pyramidal neurons in the vmPFC **well-known for their plasticity in response to environmental stimuli (Izquierdo et al., 2006)** (Fig. S1A-B, Fig. 1A). We observed significant differences between light regimes, with mice in the DD group displaying severe dendritic atrophy, with a reduction in total apical dendritic length of ~36% relative to LD controls, and a similar (~40%) significant reduction in the number of branch points (Fig. 1B-C). This shows that light is required for the normal development of the vmPFC.

Dark rearing causes depression-like mood alterations (Zhou et al., 2018) and lengthens the period of circadian rhythms in rodents (Chew et al., 2017). Depression is associated with metabolic changes in the vmPFC (Drevets et al., 1992). This raised the possibility that our DD results might have been secondary to these alterations. To address this, we used two mouse lines that detect light but lack a subset of ipRGCs (Güler et al., 2008; Chen et al., 2011). We analyzed the vmPFC pyramidal neurons of

a transgenic mouse line that expresses an attenuated form of diphtheria toxin A ("aDTA") under the control of the melanopsin promoter (*Opn4*$^{aDTA/aDTA}$). In aDTA mice, M1 ipRGCs develop and function normally until about 8 weeks of age, when they start degenerating; the loss progresses linearly with complete die-off by 6 months (Güler et al., 2008). Basal mood, as assessed by forced swim and sucrose preference tests, is normal in these animals, their visual system develops normally, and they have intact circadian rhythms (Güler et al., 2008; LeGates et al., 2012). In addition, ipRGC degeneration in aDTA mice occur without traumatic or stressful procedures known to affect PFC neuronal morphology (Izquierdo et al., 2006). In mice older than 6 months, we observed major differences between genotypes, with reconstructed neurons from aDTAs displaying severe dendritic atrophy (Fig. 1D-F), similar to what was observed in wildtype mice reared in DD. The reduced number of intersections in Scholl analysis after ipRGC loss (Fig.1D) confirmed a reduction in total apical dendritic length by ~30% in aDTA mice relative to controls (Fig.1I), with a ~36% significant reduction in the number of branch points (Fig. 1M).

The time course of ipRGC loss in aDTAs afforded an internal control. We repeated the morphometric analysis in aDTA mice at 7 weeks old, before the onset of cell degeneration, and at 3-4 months old, when ~50% of ipRGCs had degenerated. At 3-4 months of age, aDTA mice displayed an early form of the atrophic phenotype showing ~10% reduction in total apical dendritic length and ~33% reduction in number of branch points compared age matched control mice (Fig. 1H, L). In contrast, the atrophic phenotype was not observed in 7-week-old aDTA mice, when degeneration of ipRGCs had not started (Fig. 1E, G, K, J, N). Thus, the severity of apical dendritic atrophy seen in this neuronal population was proportional to the extent of ipRGC loss and confirms an essential role for light in the dendritic development of the vmPFC.

To investigate if the atrophic phenotype we observed is specific to regions of the cortex that receive ipRGC input, we reconstructed neurons in the motor cortex as a control region. No differences between the wildtype and aDTA mice in the motor cortex were observed (Fig. S1C), indicating that the atrophic phenotype was specific to the vmPFC.

Chronic dark rearing and the aDTA mice lack the ability to adjust their day/night activity to the 24-hour day in what is known as circadian photoentrainment (Chew et al., 2017; Güler et al., 2008). The lack of circadian photoentrainment could underlie the atrophic phenotype we observed in the vmPFC. Therefore, we repeated our analysis in a transgenic line, *Opn4*$^{Cre/+}$*; Brn3b*$^{zDTA/+}$ (Brn3bDTAs) mice that have normal circadian photoentrainment but lack ipRGC input to the PHb-vmPFC (Chen et al., 2011). These mice express a strong variant of diphtheria toxin A under the control of the Brn3b promoter in a Cre-dependent manner, and Cre itself under the control of the melanopsin promoter.

Brn3b is a transcription factor expressed in all ipRGCs except a subset of M1 cells that project to the SCN and are sufficient for circadian photoentrainment (Chen et al., 2011). So, Brn3bDTA mice can synchronize their circadian rhythms to the environmental light cycle but lose in developmental stages non-SCN-projecting ipRGCs. In this mouse model, we found vmPFC abnormalities identical to those present in dark reared and aDTA mice showing an ~33% average reduction in total apical dendritic length and ~37% fewer branch points vs. littermate controls (Fig. 1D, I, M). We conclude that lack of light-driven ipRGC input leads to apical dendritic degeneration in the vmPFC, and that this effect is not secondary to any SCN-based circadian disruptions, mood alterations, or developmental effects.

vmPFC response to a stressful stimulus is reduced in ipRGC-ablated mice

We then measured the activity of the vmPFC in ipRGC-ablated mice by photometry recording in freely moving mice. We transduced vmPFC neurons of Brn3bDTA mice and wildtype littermates with the Ca^{2+} sensor, GCaMP6f, under the control of the synapsin promoter. An optical fiber was implanted above the vmPFC region (Fig. 2A) and patched to a photometry apparatus capable of exciting GCaMP and measuring emitted fluorescence without restricting the movement of animals. We recorded the activity of the vmPFC at different circadian times, since the vmPFC is known to display strong circadian rhythms (Perez-Cruz et al., 2009). Contrary to the presence of strong molecular circadian clock in the vmPFC, the activity of the vmPFC did not show robust daily variations. However, the vmPFC of ipRGC-ablated animals, indeed exhibits lower activity, specifically by showing fewer endogenous activity peaks compared to controls (Fig. 2C, D). These data suggest that ipRGC input to the PHb maintain vmPFC integrity and function.

The changes in the basal activity and morphology of the vmPFC prompted us to investigate the intra-vmPFC Ca^{2+} dynamics in response to a stressful stimulus. A sudden loud sound was chosen (Fig. 2B) because it is independent of the visual system ensuring that any difference between ipRGC-ablated mice and controls could not be due directly to loss of the visual sensory input. Neuronal activity in controls and Brn3bDTAs surges after the auditory stimulation (Fig. 2E), reaching a peak ~500 ms on average after the sound is emitted, with no significant difference between genotypes on time to peak. The amplitude of the peak response was also not significantly different between genotypes. However, the time course of the decay differed significantly (Fig. 2F) in that fluorescence decayed to baseline (T_{decay}) in 4.13 s in Brn3bDTAs vs. 22.08 s in controls. This longer decay means that the cumulative activity, quantified by area under the curve (AUC), is significantly higher in controls (Fig. 2G). Thus, the absence of ipRGC input causes deficits in the vmPFC that are manifested at the morphological and neuronal activity levels and its response to stressful stimulations.

Lack of ipRGC input leads to severe gene-expression dysregulation in the vmPFC

The profound dendritic atrophy and weakened activity in the vmPFC may reflect a more generalized network-level dysfunction that would leave a characteristic transcriptomic signature. To investigate this, we performed high throughput single cell RNA-sequencing on cortical tissue from *Opn4*$^{Cre/+}$;*Brn3b*$^{zDTA/+}$ (Brn3bDTA) and littermate *Opn4*$^{+/+}$;*Brn3b*$^{zDTA/+}$ (control) mice (Fig. S2A). This line was chosen over aDTAs because it was possible to harvest tissues at a younger age that is more amenable to tissue dissociation. We generated high quality single cell transcriptome profiles for 24,340 cells (11,800 control, 12,540 Brn3bDTA) and used unsupervised learning approaches to identify over 20 transcriptionally distinct cell types within the vmPFC (Fig. S2B, C). We first identified, based on the expression of canonical marker genes, major cell types including glutamatergic neurons (*Slc17a7* a.k.a. *Vglut1*), GABAergic neurons (*Gad2*), astrocytes (*Gja1*), oligodendrocytes (*Olig1*), endothelial cells (*Flt1*), mural cells (*Rgs5*), microglia (*Selplg*), perivascular macrophages (*F13a1*), and fibroblasts (*Dcn*) (Saunders et al., 2018; Zeisel et al., 2018) (Fig. S2D). Consistently with the prior literature (Badea et al., 2009), no *brn3b* transcripts were detected in any cluster. We then extracted the identified neuronal cells and performed an additional round of unsupervised clustering to resolve 16 discrete neuron types within the vmPFC (6,914 control, 7,278 Brn3bDTA) (Fig. 3A, B).

To correlate each neuronal cluster to a specific anatomical layer of the cortex, we identified marker genes for each cluster and examined their expression in the Allen Brain Atlas ISH database (Fig. S3A-D). For 14 of these clusters, we were able to identify their origin layer based on patterns of gene expression; 10 were excitatory (*Slc17a7*-positive) and 4 were inhibitory (*Slc32a1*-positive) (Fig. 3C). Each contained cells originating from both control and Brn3bDTA tissue, though in most cases there were fewer Brn3bDTA neurons, despite their outnumbering control neurons overall (Fig. 3D). The remaining 2 neuronal clusters, on the other hand, exhibited extreme divergence (Fig. 3D). These clusters did not contain any strongly specific marker genes, appearing instead to be weakly *Slc17a7*-positive glutamatergic neurons markedly depleted of RNA content. We first ranked the most significantly differentially-expressed genes across all cell clusters, to identify those subject to the largest dysregulation in the Brn3bDTA vmPFC (Fig. 3E). We found that genes associated with neurotransmission and synaptic plasticity are severely dysregulated in the vmPFC of ipRGC-ablated mice, whereas genes associated with cell stress and immune responses are upregulated (Fig. 3E).

We then examined the two unknown clusters, U1 and U2. The largest unspecified cluster, U1, contained a striking 2,727 Brn3bDTA but only 101 control neurons. When we examined the differentially expressed genes between the U1 and the remaining clusters, we found that it was

substantially depleted of hundreds of transcripts (>900 genes, $p < 10^{-100}$) and enriched for relatively few (Fig. 3F). To see what genetic programs were depleted in these cells, we performed gene ontology analysis on all significantly upregulated or downregulated genes (Fig. 3G, H). Downregulated genes were involved in pathways including ion channel activity, ion transport, nervous system development, and many other canonical neuronal functions. Conversely, within the upregulated set of genes in U1, we detected signatures of cellular stress and/or degeneration including unfolded protein binding and pathways implicated in Huntington's and Parkinson's disease. Thus, it appears that cluster U1 neurons, overwhelmingly from Brn3bDTA animals, broadly downregulate normal neuronal processes in a shift to stress-related responses. The smaller unknown cluster, U2, containing predominantly control neurons (8 Brn3bDTA, 297 control), shared a similar set of genes as measured by gene ontology (Fig. S3E) but downregulated to a much less significant degree (Fig. S3F, G). Together our analyses showed large changes in genes involved in synaptic plasticity and signaling specifically in ipRGC ablated animals.

To determine whether the effect of ipRGC loss was specific to the vmPFC, we collected tissue from the nearby motor cortex in both control and Brn3bDTA animals and repeated the scRNAseq analysis. Again, we could identify all major cell types from both control and Brn3bDTA tissue in the motor cortex. Among neurons, we saw an even overlap and distribution of neuronal cell types, with no large cluster containing degenerate neurons or an enrichment of Brn3bDTA cells (Fig. S4A, B). Thus, we can confirm that the detrimental effect of ipRGC loss was indeed specific to the vmPFC.

ipRGC-ablated mice show impaired regulation of aversive emotions

ipRGC-ablated mice have normal mood, as assessed by forced swim and sucrose preference tests, and their hippocampal-dependent memory is unimpaired (Fernandez et al., 2018). Prefrontal injuries in humans show changes in general cognition and social demeanor, and in both primates and rodents, prefrontal cortex lesions result in anomalous social behavior (Brody & Roxvold, 1952, Sato, 1971, Franzen & Myers, 1973). We opted, therefore, to examine the behavior of ipRGC-ablated mice in a social context. The ipRGC-ablated and littermate control animals were housed in standard colony conditions with their same-sex littermates for at least 6 months and no exposure to females after weaning. Male mice were tested in a free social interaction test (Fig. 4A) in which the mouse was exposed for 5 minutes in an unfamiliar setting to a strange conspecific of the same sex. The interactions between the two mice were tracked and scored for many different parameters of social behavior, including total time interacting together. Moreover, since we have noticed in our lab that socially isolated aDTA mice become hyper-reactive relative to wildtypes, and social isolation is a known stressor to rodents capable of altering PFC myelination patterns (Liu et al, 2012), we tested mice before

social isolation (Fig. S6B), after a short 4-day period of social isolation, and again after long-term 23-day isolation (Fig. 4A).

After long-term isolation, ipRGC-ablated mice substantially reduced social interactions with their conspecific (Fig. 4B) by avoiding the conspecific when approached and were averse to interacting closely by spending less time engaging in social behaviors such as nose-touching and sniffing (Fig. 4B, C, Supplementary Video 1). As these mice were never exposed to females, there was little immobility and severe fighting was uncommon (Fig. S6A). Thus, the decreased social interactions (Fig. 4C) were not due to aggressive behavior.

To assess social preference further, we used the 3-chamber test, where a mouse is given a choice between a conspecific and an object (Fig. S5A). ipRGC-ablated mice were significantly less likely to spend time in the conspecific-mouse compartment during the first 2 minutes of the trial—consistent with heightened fear towards unfamiliar conspecifics displayed in the free interaction assay (Fig. S5B and C, Supplementary Videos 2, 3). The reduced social contact exhibited by the ipRGC-ablated mice suggested to us an increased state of generalized anxiety. We first used the marble burying test and measured defensive burying of 20 marbles perceived as a potential threat. The number of marbles buried by ipRGC-ablated mice was not different to littermate controls (Fig. S6C) confirming that ipRGC ablation does not heighten fear towards potentially threatening stimuli.

We then subjected the ipRGC-ablated mice to the looming test, where fear is induced by stimulating a predator attack. In this test, mice typically react to an expanding dark disc used to mimic a predator approaching or looming from above by escaping to the shelter, freezing or rattling their tails (Fig. 4D, Supplementary Video 4). Tail rattling during the looming test is directly mediated by the medial PFC (Salay et al., 2018), and has been used as a proxy for social fear associated with prefrontal cortex dysregulation, whereas the shelter escape and the freezing behaviors are dependent on image-forming vision. Consistent with previous data, the ipRGC-ablated mice showed normal image functions as they escaped to the shelter and froze in a similar proportion to their littermate controls (Fig. 4E). Remarkably, the ipRGC-ablated mice were significantly less prone to rattling their tails (only 20.0% of ipRGC-ablated mice did vs 57.1% of controls, Fig. 4E), indicating a dysfunction in the medial PFC.

We then used the defensive burying assay using a noxious odor stimulus, a behavior that is independent of image-forming functions, but still depends on the vmPFC (De Boer & Koolhaas, 2003). In this test (Fig. 4F), a Q-tip dipped in concentrated fox-urine odorant (TMT) was placed in the cage (Fig. S6D). As expected, the mice buried the Q-tip as a defensive strategy except that only 40% of the ipRGC-ablated mice buried within the 20-minute limit of the test relative to 80% of the wildtypes (Fig. 4G). The ipRGC-ablated mice also took significantly longer to bury the Q-tip relative to controls (650

vs. 270 seconds) (Fig. 4H). Moreover, these mice typically distanced themselves from the Q-tip, often confining themselves to the opposite end of the arena (Supplementary Video 5). Thus, an olfactory stimulus elicited behavioral abnormalities just like visual stimuli did. Together, these data indicate that the behavioral deficits observed in ipRGC-ablated mice are not due to sensory dysfunction, but instead are a manifestation of emotional dysregulation due to an impaired vmPFC.

We also tested mice for high-order cognitive processing of focused attention and flexibility using a classic vmPFC test, the IntraDimensional/ExtraDimensional (ID/ED) set shifting task (Heisler et al., 2015). Briefly, mice were trained to dig into ramekins for a buried pellet of food. The ramekins were filled with different digging media, and during the test (Fig. 4I), the mouse performed a series of discriminations that differed along two dimensions (i.e., odor and texture). Two measures of performance were recorded: a) the number of trials to reach a criterion level of performance as a measure of accuracy, and b) the latency to correct their choice following an error (counter choice). In the Simple Discrimination (SD) stage, the mouse learnt that a specific digging medium was associated with reward. In the subsequent Compound Discrimination (CD) phase, an additional dimension was introduced; now the ramekins differed by both digging medium and scent, but the mouse must focus on the digging medium as the relevant cue. In the Reversal (Rev) stage, the reward contingency was reversed such that the previously unrewarding scent was now rewarded. In all these stages of learning, (SD, CD and Rev) the ipRGC-ablated mice and the controls did not differ in their performance (Fig. 4J, and Fig. S5D) indicating normal learning capabilities in ipRGC-ablated mice.

We then subjected the mice to the IntraDimensional Shift (IDS) during which the mice were required to discriminate three new exemplars of digging media/odors (IDS1, IDS2, and IDS3). In all cases, the reward was associated with the digging media and not the odor. For the most part, the animals performed normally on the IDS discriminations with no major changes between the ipRGC-ablated mice and the controls in terms of accuracy and the latency to counter-choice (Fig. 4J, and Fig. S5D). We observed an unexpected deficit in IDS2 rule acquisition because the animals were trained in this stage on the following day (Fig. S5D). The main difficulty, however, came during the ExtraDimensional Shift (EDS) test when for the first time in the course of testing, odor become the rewarding stimulus and the digging medium had to be ignored. Now the ipRGC-ablated mice were markedly impaired, evidenced by long latencies to make their response to the new rewarding dimension (Fig.4J). Performance in this complex cognitive task is linked to specific prefrontal areas: The Rev stage recruits an orbitofrontal network, while the EDS relies on the medial portions of the PFC. Therefore, our data indicate that cognitive networks in the orbitofrontal and dorsomedial PFC are

normal, and importantly, the deficits in the vmPFC we observed are not due to a generalized prefrontal dysfunction.

Discussion

We report, using two genetic lines and constant dark rearing, that light via ipRGCs affects the activity and function of vmPFC in mice, independent of circadian, developmental, and mood alterations. Using a genetic line (Brn3bDTA mice), which has normal circadian photoentrainment since only non-SCN projecting ipRGCs are ablated at early stages, we uncover that the effects of ipRGCs on vmPFC are not a corollary of circadian disruptions. In addition, using a genetic line (aDTA mice) where ipRGCs are ablated only at adult stages starting at 2 months and completed by ~6 months (Güler et al., 2008), we demonstrate similar deficits to those of Brn3DTA mice, indicating that there is no developmental critical period for the effects of ipRGCs on vmPFC. Finally, both genetic lines show normal basal mood as assessed by classical depression tests (Fernandez et al., 2018; LeGates et al., 2012), highlighting that the effects of ipRGCs on vmPFC are not a consequence of mood alterations. Importantly, even in the presence of ipRGCs, the absence of light (dark rearing) leads to similar deficits in the vmPFC dendritic structures as those observed in the two ipRGC-ablated genetic lines.

We decided to investigate the vmPFC because it receives input from the PHb that is innervated directly by ipRGCs (Fernandez et al., 2018). In this study, we refer to the PHb-recipient area of the prefrontal cortex, broadly encompassing the infralimbic and prelimbic cortex, as vmPFC (Hiser & Koenigs, 2018). Previously, it was shown that the PFC dendritic structure of pyramidal neurons are sensitive to circadian disruptions and stress (Perez-Cruz et al., 2009), with stress inducing the largest deficits. Remarkably, the deficits in the dendritic structures we observe in this study, using the two genetic lines and dark rearing, are greater than those observed with stress. Simply ablating ipRGCs or just depriving a nocturnal animal from light led to changes in the vmPFC that are more substantial than stress or circadian disruptions. We also investigated the timecourse of the changes in the dendritic structures and correlated them to ipRGC loss in aDTA mice. We observed that deficits in the dendritic structures of pyramidal neurons directly correspond with the extent of ipRGC loss, showing normal morphology at ages below 2 months and then showing progressive disruptions starting at 3-4 months. The morphological changes we observed are correlated with physiological deficits in the response of the vmPFC to acute stressors such a loud sound. The use of a noxious auditory stimulus avoids the complications of using a retina-dependent stressor. We used photometry to show that vmPFC of ipRGC-ablated animals respond initially to the sound but show faster decay and smaller area under the

curve in response to the acute stressor. Our studies indicate that ipRGCs of the retina, and their light reception has a profound influence on the morphology and the physiology of the vmPFC.

Neurons within the vmPFC are relatively plastic and respond to a variety of stressors and behavioral manipulations. For our single cell sequencing analysis from both control and ipRGC-ablated animals, most neurons are healthy and layer specific. However, we observed two unspecified clusters (U1 and U2), with most cells in U1 hailing from ipRGC-ablated animals. Both the U1 and U2 clusters represent a regressed neuronal state, rather than a neuron type, that normally exists within the vmPFC in adult animals. Remarkably, in ipRGC-ablated animals the numbers of cells with regressed neuronal state were substantially higher with thousands of them appearing in the U1 cluster. Within scRNA-seq experiments there are often large number of reads generated from ambient RNA binding to transcriptome capture beads, which when sequenced create the illusion of real cells with low gene content. These low-quality cells often contain very few genes that are of mixed origin between major cell types. Importantly in our case, the U1 and U2 all contain a strong complement of genes (>500 each) and are not positive for non-neuronal cell type markers. For this reason, we have categorized these cells as unhealthy neurons. Specifically, for U1 cluster, the general decrease in neurons with layer- or type-specific genetic signatures was accompanied by a striking increase in gene-poor neurons that likely represent degenerate cells. This observation is in strong agreement with histological data taken from the vmPFC of ipRGC-ablated animals which show a substantial retraction of pyramidal apical dendrites compared to wildtype littermate controls. This dendritic retraction nicely matches the genetic retraction that we see in U1, which are significantly depleted for over 1000 genes. These downregulated genes even show expected signatures of dendritic atrophy including GO terms associated with synapses, cell membrane, and cell adhesion. For example, inhibitory interneuron markers (Gat1, Gad1 and -2, Cnr1, Kcnc1 and -2, Vgat) were the most downregulated genes, followed by regulators of synaptic transmission, synaptogenesis and dendritic outgrowth, and neuronal excitability (Neurexins, Hcn1, GluA1, Tenm2, Elavl2, Cntnap2); the most relatively upregulated genes were signatures of cell stress, inflammation, or immune system reactivity, with the exception of Npas4, a transcription factor that regulates the number and distribution of inhibitory synapses on dendritic arbors (Bloodgood et al., 2013).

In rodents, the prefrontal cortex is important for social behaviors. We have conducted several behavioral tests (free interaction and 3- chamber) to examine the social behavior of the animals lacking input to the PHb, and a selected set of behaviors (Looming, Defensive Burying and Attention Set Shift tests) that are known to be associated with the medial PFC. Animals lacking input to the PHb showed severe social dysregulation. This emotional dysregulation was not due to an increased state of

generalized anxiety (Marble Burying Test), in agreement with previous studies (LeGates et al., 2012). The Looming, Defensive Burying, and Attention Set Shift tests measure mPFC function directly. The Looming is particularly informative because it measures two aspects, vision, by the freezing and sheltering of the mouse and mPFC function by the tail rattling. Remarkably, animals lacking input to the PHb showed deficits only in tail rattling, indicating cortical vision to be intact. Defensive Burying test, a non-visual behavior for the mPFC function, further confirmed that the deficits in the mPFC are not due to cortical visual effects. Finally, the most comprehensive test was the Attention Shift Set, which measure 7 aspects that involves memory and discrimination, and the animals lacking input to the PHb only showed deficits in the EDS stage, which is highly dependent on the medial portions of the PFC, but not the Rev stage, which is dependent on the orbitofrontal region that does not receive input from ipRGCs. The light-modulated circuit appears to be mainly involved in the top-down regulation of negative emotions, possibly via an attentional effect, as revealed by the performance of ipRGC-ablated mice in the EDS stage of the attention set shift test. Based on the impaired rule-acquisition of ipRGC-ablated animals in the IDS2 stage of the same test, a deficit in the retention of procedural memory also cannot be ruled out; it has been suggested that the PFC may mediate “episodic control”, i.e. the storage of a rule in memory and its use to adapt behavior (Koechlin et al., 2003). These results show that the morphology, physiological and molecular deficits in the vmPFC lead to medial PFC specific behavioral deficits.

Our results allow for a simple model. Light through ipRGCs that innervate the PHb activates the vmPFC, and this activation is important for the integrity of the morphological, physiological and molecular components of the vmPFC. Our discovery of modulation by light of the vmPFC raises an intriguing possibility. The PFC is the most evolutionarily recent area of the neocortex, and its most primordial core is the vmPFC. Its modulation by ipRGCs, simple photodetectors found in all vertebrates, invites the speculation that its evolutionary origin and ancestral function may lie in the regulation of light-driven daily activity patterns.

A striking aspect of this study is the fact that dark rearing led to major deficits in the vmPFC. Dark rearing has been shown to affect the primary visual cortex. However, this is not surprising considering the massive input from the retina to the primary visual cortex. But are the deficits in dark rearing occur secondarily through the primary visual cortex? Remarkably, animals that lack only ipRGCs and have normal input to the primary visual cortex still exhibit deficits in the vmPFC, even though the PFC receives input broadly from sensory areas, including visual ones (Noudoost et al., 2021). Therefore, the absence of an ancient photoreceptive system that is subconscious in nature is sufficient to cause deficits in the vmPFC, even in the context of functional cortical vision.

In humans, the PFC expands during development eventually adding up to 29% of the overall volume of the cortex (Brodmann, 1912), a large proportion to total brain size, which sets a record for the entire animal kingdom (Uylings & Van Eden, 1990). It is well established in the literature that the PFC is one of the first brain region to undergo age-dependent degeneration, a phenomenon characterized by morphological changes (dendritic atrophy) strikingly similar to those observed in this study after light deprivation. Aging causes a progressive yellowing of the eye lens, an effect that reduces the intensity of blue-shifted light reaching the retina. It was shown that the transmission of 480 nm light decreased by 72% at age 80 relative to age 10 (Kessel et al., 2010). It is precisely to these short-wavelength photons that ipRGCs are most responsive. The outcome is an age-dependent, progressive loss of ipRGC signaling. This was thought only to result in the characteristic circadian and sleep disturbances seen in the elderly. We may now have reason to suspect a role of ipRGC signaling in PFC age-dependent degeneration.

A marked trend in recent decades has been the proliferation of artificial blue-light sources, and human nighttime exposure to them, an unprecedented behavior in the natural history of our species known to disrupt physiological ipRGC signaling. The emotion-regulatory function of the vmPFC is specifically affected in many disorders, from schizophrenia to autism to syndromes characterized by fear generalization (Hiser & Koenigs, 2018). Some of the most dysregulated genes in the PFC of mice lacking ipRGC signaling (e.g., *cntnap2*) are mutated in well-established mouse models of such disorders (Ellegood & Crawley, 2015). More generally, in this study we show that light, via a retinal cell population, profoundly affects the prefrontal cortex across multiple domains—neuronal morphology, gene expression, network activity, and behavior—, with effect sizes so considerable as to suggest an ecologically important regulation. This unexpected feature, if confirmed in humans, may prove to be of considerable interest.

Materials & Methods

Animals

Opn4$^{aDTA/aDTA}$ and *Opn4*$^{Cre/+}$*;Brn3b*$^{zDTA/+}$ mouse lines were used in this study, housed under a 12 h light: 12 h dark (T24) cycle at a temperature of 22--25°C with food and water ad libitum unless otherwise noted. In Brn3bDTAs, ~200 ipRGCs survive per retina, which are the only ipRGCs that do not express the transcription factor Brn3b (POU4F2); these cells exclusively innervate the SCN. Brn3bDTA mice were obtained by mating mice that express the Cre-dependent diphtheria toxin under the control of the Brn3b promoter (Brn3b$^{zDTA/+}$), with Opn4$^{Cre/Cre}$ mice. Opn4$^{Cre/+}$ littermates were used as controls. All

animals were handled in accordance with guidelines of the Animal Care and Use Committees of Johns Hopkins University and the National Institutes of Health.

Golgi staining and cell morphometry

Animals were socially housed with littermates in standard colony conditions till the indicated age; rapidly anesthetized with 5% isoflurane, their brain was extracted without any preliminary fixation, rinsed with PBS, and processed with FD Neurotechnologies' Rapid Golgi staining kit, in accordance with the kit protocol. The resulting 200-mm coronal sections were imaged at 40x to 100x magnification. The dendritic morphology of neurons in the Golgi-stained sections was reconstructed using the Neurolucida tracing system (MicroBrightField). The neurons to be traced were selected according to the following criteria: 1. Position in the prefrontal cortex area shown by previous tracing to receive PHb afferents (PL and IL cortices). 2. Pyramidal type, with a roughly triangular soma, a clear single apical dendrite extending from the soma towards the pial surface, and two or more dendritic trees extending from the base of the soma. 3. Distance from the soma to the pial surface <390 µm and >280 µm (~layer 3). 4. Shape of the apical dendritic tree not suggestive of a layer 5 or short-shaft layer 2/3 neuron. 5. Apical dendritic tree mainly unfolding within the middle third of the section, well isolated and not obscured by neighbors. 6-10 cells typically qualified to be analyzed per animal (with little discretion for the experimenter). The cells were traced and reconstructed by two independent investigators, one of whom was blind to genotype. Analysis of the variables of interest was performed automatically by Neurolucida Explorer.

Single-cell RNA sequencing

Generation of single cell suspensions from vmPFC tissue

1-month-old Brn3b^{zDTA} animals and littermate controls were used for scRNA-seq experiments. The brain was extracted after rapid anesthesia induction with 5% isoflurane. The vmPFC was manually excised and the cells dissociated according to a published protocol (Saxena et al., 2012). Cell viability was measured with Trypan blue and resuspended in ice-cold PBS to desired concentrations for 10X Genomics single cell capture.

Data analysis

Single cells were loaded into a 10X Genomics Chromium controller and processed with the 3' single cell gene expression solution V2 (10X Genomics) according to manufacturer instructions. Up to 3 libraries were multiplexed at once and sequenced on an Illumina Next-Seq500 platform. Reads were

demultiplexed and aligned and digital gene expression matrices were generated with the CellRanger pipeline from 10X Genomics. Read demultiplexing and alignment was performed on the Maryland Advanced Research Computing Center (MARCC), and data analysis was performed on local Mac/Linux devices using the Seurat package in R.

Digital gene expression matrices for each replicate were loaded into Seurat, retaining only cells that expressed at least 500 unique genes. Samples from both genotypes were scaled, normalized, and integrated for comparative analysis in Seurat(Stuart, Butler et al., 2019). We then performed principal component analysis with uniform manifold approximation and projection (UMAP), and clustering by k-nearest neighbor method to reveal distinct clusters. Cluster identities were determined by differential expression of distinct cell-type specific markers. For detailed analysis of individual cell types, cells of interest were extracted and reprocessed following the same procedure.

Gene Ontology analysis

Gene ontology analysis was performed using the Database for Annotation, Visualization and Integrated Discovery (DAVID) (Huang et al., 2009).

Bulk gene dysregulation ranking

A subset of data from high-quality, non-RNA-depleted cells only was used for this analysis.

Fiber Photometry

Mice were maintained under 1-1.5% isoflurane anesthesia, and stereotactically injected with 120 nL of AAVDJ-syn-GCaMP6f, titer 10^{12} gc/mL, over approximately 10 minutes. The empirically-optimized injection coordinates were ML 0.15, AP 1.72, DV 2.84-2.64, relative to bregma; the DV coordinate was adjusted for each animal (the goal being to inject 2±0.1mm from the dorsal surface of the brain). An optical fiber ⌀400mm with conical tip (Doric Lenses) was implanted over the injection site, in the PL cortex (DV ~2.5) (See Fig. S4A). After 5 weeks, the animals were transferred into a special cage and connected to a photometry apparatus (Doric Lenses), where all experimental manipulations were conducted. Ca^{2+}-dependent and isosbestic fluorescence wavelengths were recorded, the latter as an internal control. Every trace was rectified and corrected by fitting first for exponential decay and secondly linearly using the isosbestic fluorescence as the regressor. A classic problem with photometry is inter-individual comparisons, as many hard-to-control-for variables affect even normalized fluorescence amplitude (e.g. transfection efficiency, distance of transfected cells from fiber tip,

differences sometimes in LED optical power output). To get around this hurdle, we took advantage of the “background noise” produced, in each recording, by uncorrelated single-cell activity at rest. We calculated the median absolute deviation (MAD) of stretches of such minimal activity for every trace and equalized them across animals. **The possibility of differential GCaMP expression between groups, which would result in different amplitude of this activity, was thus accounted for.** MAD normalization affects only measures of fluorescence amplitude, not time- or frequency- based variables. Recordings from mice in which the transfection site was subsequently found to be outside the ILC were excluded (these recordings typically did not show sound- and/or light- evoked responses). All the mice used in this experiment had completed the behavioral tests described below and were 11 to 13 months old (age-matched between genotypes).

RNA Scope

We initiated the experimental procedure by meticulously cleaning our tools, slides, and equipment using a 70% ethanol solution combined with ribonuclease inhibitors (Fisher Scientific). Subsequently, we humanely euthanized the mice (2 Control and 3 DTA) through cervical dislocation and promptly dissected their brains, flash-freezing them in 2-methylbutane that was pre-chilled on dry ice for a duration of 20 seconds. These frozen brains were then securely stored at -80°C until the time of sectioning. The brain sectioning process was carried out utilizing a cryostat from Leica, generating sections of 20 µm in thickness which were then affixed onto microscope slides. These slides, bearing the brain sections, were stored at -80°C until we were prepared for the in-situ hybridization procedure. For the in-situ hybridization, we followed the standard protocol as outlined by the manufacturer, employing the RNAscope™ Intro Pack for HiPlex12 Reagents Kit (488, 550, 650) - Mm v2, provided by Advanced Cell Diagnostics (ACD, Cat. #324443). The sections on the slides were initially fixed with 4% paraformaldehyde for a duration of 60 minutes at room temperature. Following fixation, the slides underwent two consecutive 1-minute washes with PBS before undergoing a dehydration process involving 50% ethanol (1 × 5 min), 70% ethanol (1 × 5 min), and two rounds of 100% ethanol (2 × 5 min each). Subsequently, the slides were placed in 100% ethanol at -20°C overnight. On the following day, the slides were allowed to air-dry at room temperature for a period of 10 minutes. A hydrophobic pen was used to delineate a hydrophobic barrier around the sections and was allowed to dry for an additional 10 to 15 minutes. The sections were then treated with Protease Pretreat-4 solution for 30 minutes at room temperature. After this, the slides were washed twice with ddH2O (2 × 1 min each) before being incubated with the appropriate probes. The probes for the eight target genes were procured from Advanced Cell Diagnostics and included Mm-Nlgn2 (T2; 406681), Mm-Ubb (T8; 591071), Mm-

Hspa8 (T7; 1137391), Mm-Pfn2 (T6; 559691), Mm-Gls-O1 (T4; 535651), Mm-Map2 (T3; 431151), Mm-Gad2 (T5; 439371), and Mm-Cntnap2 (T1; 449381). These probes were hybridized to the sections for a period of 2 hours at 40°C, followed by washing and hybridization with target-binding amplifiers to facilitate signal amplification for the detection of single RNA transcripts. In the initial round of hybridization, the first three of the twelve target genes (T1-T3) were labeled with three distinct fluorophores. Subsequently, the sections were counterstained with DAPI for 30 seconds and mounted with ProLong Gold Antifade Mountant (Jackson ImmunoResearch, Cat. #017-000-121). Image acquisition was carried out using an ECLIPSE Ti2 inverted microscope from Nikon. After imaging the sections, the coverslips were removed in 4X SSC buffer (G. Biosciences, Cat. #786-023), and the fluorophores were cleaved using the cleaving solution provided in the kit. This process was repeated iteratively, targeting sets of three genes at a time (T4-T6, T7-T9), until all eight target genes were successfully imaged and analyzed.

The procedure for image involved several steps. First, each confocal image file was imported into FIJI ImageJ. Subsequently, a maximum intensity z-projection was generated. Following this, each channel within the image was separated into distinct image files, and each newly created image was saved in the TIFF file format. To align and combine images obtained from multiple rounds of tissue imaging, we utilized the ACD Biosciences Image Registration Software, following the manufacturer's specified protocol as outlined in ACD Biosciences Document No. 30065UM. In a concise summary of the process, one of the DAPI images from the various rounds of imaging served as the reference image. All other DAPI images from subsequent imaging rounds were registered to this reference image. This registration process produced a transformation matrix that contained coordinate conversions, which were subsequently applied to all the other gene-specific images and images from each round of imaging. This step effectively established a unified coordinate system for all images from all imaging rounds. Within the same software tool, we also cropped non-overlapping regions present around the edges of the images. Following cropping, each registered image was saved separately as a TIFF file.

To quantify the data, we standardized our approach by selecting a uniform region of interest (ROI) for each section. These ROIs were chosen to cover an equivalent area encompassing layers I-III of the ventromedial prefrontal cortex (vmPFC), as illustrated in Figure S7. Subsequently, in ImageJ, a manual threshold was applied to each image, leading to the creation of binary images. The count of positively

stained pixels within these binary images served as our measure of the average signal, which was then subjected to statistical analysis.

Behavioral Tests

Tests were performed during the mice's active phase under dim red light. In every case, the animals were habituated by keeping them at least 1 h in the test room before the test was performed. All test sessions, except for IDED, were videotaped and every single video is available for the reader's viewing pleasure at the link provided in the next section. Particularly salient examples are enclosed here as Supplementary Material. IDED sessions require 5 to 10 hours' total time per animal, and were therefore not recorded, except for the representative snippets in Supplementary Material. All tests were performed with the experimenter blind to genotype.

Free Interaction Test

The test mouse was placed in an unfamiliar cage with new bedding, acclimatized for 20 minutes, and exposed for 5 minutes to a strange wildtype conspecific of the same sex of approximately 7-12 weeks of age. Neither participant was a breeder mouse (to reduce aggression). Interactions between mice were analyzed by TopScan (CleverSys, Inc).

3-Chamber Test

The test mouse was placed in the middle chamber and acclimatized for 10 minutes, then partitions were removed allowing the animal to explore the other 2 chambers, for 10 minutes. Again, movements were analyzed with TopScan.

Marble Burying Test

The mouse was dropped into a square-footprint arena with 10-cm-thick corncob bedding and a regular array of 20 1-cm black marbles. After 10 minutes, he was extracted from the cage and the number of completely or partially buried marbles counted.

Looming Test

As previously described, the test mouse was placed in a custom-built arena and allowed to acclimatize for 10 minutes. A maximum of 10 iterations of the expanding disc animations were played (the series was cut short if the mouse displayed all the three behaviors of interest).

Defensive Burying Test

Mice were acclimatized to the unfamiliar test cage, with a 5-cm-thick layer of new bedding, for 10 minutes. A Q-tip soaked in 4 mL of TMT was dropped into the cage in the second quadrant, and the mouse's reactions videotaped for 20 minutes.

IDED Test

Every mouse was preliminarily handled by the experiment for 7 days, and weighed to determine a body weight baseline. Food restriction followed, for 4 days, with 1 to 2 g of food dispensed every day in the ramekins subsequently used for the test. Then the mice were acclimated to the test arena for 2 days; and trained to dig into bedding-filled ramekins for food for 1 or 2 days depending on performance. Body weight typically dropped to 80% of baseline by the beginning of the test sessions.

Statistical Analysis

Statistical analysis of results was made by a Student's t test or a two-way analysis of variance (ANOVA), unless otherwise stated.

Data Availability

All videos of recorded behavioral tests, as well as all original databases, are freely and publicly available at https://livejohnshopkins-my.sharepoint.com/:f:/g/personal/llazzer1_jh_edu/ElJEwX1ivCxBgmIAeyz27D4BLs4iGfZFEnHA8_WJjOOlFg?e=QIHj7D.

Acknowledgments

This work was supported by NIH grants GM076430 and EY027202, the Intramural Research Program of the National Institute of Mental Health (MH002964 to SH and ZIA MH002951 to YC) and the Rodent Behavioral Core (ZIC MH002952). We thank Dr. Daniel Pine and Dr. Jacqueline N. Crawley for their very insightful suggestions on the behavioral phenotypes. We also thank Dr. Drew Lowery and Dr. David Adamovich for their kind support. The authors declare no financial conflict of interests.

Authors' Contributions

LLO designed the experiments, performed and analyzed the fiber photometry experiments, performed the behavioral tests. LLO and JZ performed the morphometric analysis. HW provided the animals with

the correct littermate controls. JZ and LLO performed the single-cell RNA sequencing experiments. MT and JZ analyzed the single-cell RNA sequencing data. LLO, JZ JH and KC analyzed the behavioral tests. LLO, JZ, MT, YC, HZ and SH wrote the manuscript. YC, HZ and SH discussion and guidance.

References

Adhikari, A., Lerner, T. N., Finkelstein, J., Pak, S., Jennings, J. H., Davidson, T. J., Ferenczi, E., Gunaydin, L. A., Mirzabekov, J. J., Ye, L., Kim, S. Y., Lei, A., & Deisseroth, K. (2015). Basomedial amygdala mediates top–down control of anxiety and fear. *Nature*, *527*(7577), 179. https://doi.org/10.1038/NATURE15698

Badea, T. C., Cahill, H., Ecker, J., Hattar, S., & Nathans, J. (2009). Distinct Roles of Transcription Factors Brn3a and Brn3b in Controlling the Development, Morphology, and Function of Retinal Ganglion Cells. *Neuron*, *61*(6), 852–864. https://doi.org/10.1016/J.NEURON.2009.01.020

Bianchi, L. (1922). The Mechanism of the Brain and the Function of the Frontal Lobes. *Journal of Mental Science, 68(283), Quoted in Fuster, J. (2015), "The Prefrontal Cortex", 5th Edition.*

Bloodgood, B. L., Sharma, N., Browne, H. A., Trepman, A. Z., & Greenberg, M. E. (2013). The activity-dependent transcription factor NPAS4 regulates domain-specific inhibition. *Nature*, *503*(7474), 121–125. https://doi.org/10.1038/nature12743

Brodmann, K. (1912). Neue Ergebnisse über die vergleichende histologische Lokalisation der Grosshirnrinde mit besonderer Berücksichtigung. *Anat. Anzeiger. 41, 157-216. Quoted in Fuster, J. (2015). "The Prefrontal Cortex", 5th Edition.*

BRODY, E. B., & ROXVOLD, H. E. (1952). Influence of prefrontal lobotomy on social interaction in a monkey group. *Psychosomatic Medicine*, *14*(5), 406–415. https://doi.org/10.1097/00006842-195209000-00007

Chen, S.-K., Badea, T. C., & Hattar, S. (2011). Photoentrainment and pupillary light reflex are mediated by distinct populations of ipRGCs. *Nature*, *476*(7358), 92–95. https://doi.org/10.1038/nature10206

De Boer, S., & Koolhaas, J. (2003). Defensive burying in rodents: ethology, neurobiology and psychopharmacology. *European Journal of Pharmacology*, *463*(1–3).

De Bruin, J. P. C., Van Oyen, H. G. M., & Van De Poll, N. (1983). Behavioural changes following lesions of the orbital prefrontal cortex in male rats. *Behavioural Brain Research*, *10*(2–3), 209–232. https://doi.org/10.1016/0166-4328(83)90032-3

Drevets, W. C., Videen, T. O., Price, J. L., Preskorn, S. H., Carmichael, S. T., & Raichle, M. E. (1992). A functional anatomical study of unipolar depression. *The Journal of Neuroscience*, *12*(9), 3628. https://doi.org/10.1523/JNEUROSCI.12-09-03628.1992

Ecker, J. L., Dumitrescu, O. N., Wong, K. Y., Alam, N. M., Chen, S.-K., LeGates, T., Renna, J. M., Prusky, G. T., Berson, D. M., & Hattar, S. (2010). Melanopsin-Expressing Retinal Ganglion-Cell Photoreceptors: Cellular Diversity and Role in Pattern Vision. *Neuron*, *67*(1), 49–60. https://doi.org/10.1016/j.neuron.2010.05.023

Fernandez, D. C., Fogerson, P. M., Lazzerini Ospri, L., Thomsen, M. B., Layne, R. M., Severin, D., Zhan, J., Singer, J. H., Kirkwood, A., Zhao, H., Berson, D. M., & Hattar, S. (2018). Light Affects Mood and Learning through Distinct Retina-Brain Pathways. *Cell*, *175*(1), 71-84.e18. https://doi.org/10.1016/j.cell.2018.08.004

Fogerson, P. M. (2015). *Output streams of intrinsically photosensitive ganglion cells: Distinct types supply different visual and limbic networks*.

Franzen, E. A., & Myers, R. E. (1973). Neural control of social behavior: prefrontal and anterior temporal cortex. *Neuropsychologia*, *11*(2), 141–157. https://doi.org/10.1016/0028-3932(73)90002-x

Fuster, J. (2001). The Prefrontal Cortex—An Update. *Neuron*, *30*(2).

Güler, A. D., Ecker, J. L., Lall, G. S., Haq, S., Altimus, C. M., Liao, H.-W., Barnard, A. R., Cahill, H., Badea, T. C., Zhao, H., Hankins, M. W., Berson, D. M., Lucas, R. J., Yau, K.-W., & Hattar, S. (2008). Melanopsin cells are the principal conduits for rod–cone input to non-image-forming vision. *Nature*, *453*(7191), 102–105. https://doi.org/10.1038/nature06829

Heisler, J. M., Morales, J., Donegan, J. J., Jett, J. D., Redus, L., & O'connor, J. C. (2015). The attentional set shifting task: A measure of cognitive flexibility in mice. *Journal of Visualized Experiments*, *96*. https://doi.org/10.3791/51944

Hiser, J., & Koenigs, M. (2018). The Multifaceted Role of the Ventromedial Prefrontal Cortex in Emotion, Decision Making, Social Cognition, and Psychopathology. *Biological Psychiatry*, *83*, 638–647. https://doi.org/10.1016/j.biopsych.2017.10.030

Huang, D. W., Sherman, B. T., & Lempicki, R. A. (2009). Systematic and integrative analysis of large gene lists using DAVID bioinformatics resources. *Nature Protocols*, *4*(1), 44–57. https://doi.org/10.1038/nprot.2008.211

Izquierdo, A., Wellman, C. L., & Holmes, A. (2006). Brief Uncontrollable Stress Causes Dendritic Retraction in Infralimbic Cortex and Resistance to Fear Extinction in Mice. *Journal of Neuroscience*, *26*(21), 5733–5738. https://doi.org/10.1523/JNEUROSCI.0474-06.2006

Kessel, L., Lundeman, J. H., Herbst, K., Andersen, T. V., & Larsen, M. (2010). Age-related changes in the transmission properties of the human lens and their relevance to circadian entrainment. *Journal of Cataract and Refractive Surgery*, *36*(2), 308–312.

https://doi.org/10.1016/J.JCRS.2009.08.035

Koechlin, E., Ody, C., & Kouneiher, F. (2003). The Architecture of Cognitive Control in the Human Prefrontal Cortex. *Science*, *302*(5648), 1181–1185. https://doi.org/10.1126/science.1088545

Koolhaas, J. M., de Boer, S. F., Coppens, C. M., & Buwalda, B. (2010). Neuroendocrinology of coping styles: Towards understanding the biology of individual variation. *Frontiers in Neuroendocrinology*, *31*(3), 307–321. https://doi.org/10.1016/J.YFRNE.2010.04.001

Lazzerini Ospri, L., Prusky, G., & Hattar, S. (2017). Mood, the Circadian System, and Melanopsin Retinal Ganglion Cells. *Annual Review of Neuroscience*, *40*(1), annurev-neuro-072116-031324. https://doi.org/10.1146/annurev-neuro-072116-031324

LeGates, T. A., Altimus, C. M., Wang, H., Lee, H.-K., Yang, S., Zhao, H., Kirkwood, A., Weber, E. T., & Hattar, S. (2012). Aberrant light directly impairs mood and learning through melanopsin-expressing neurons. *Nature*, *491*(7425), 594–598. https://doi.org/10.1038/nature11673

Morgan, M., Romanski, L., & LeDoux, J. (1993). Extinction of emotional learning: contribution of medial prefrontal cortex. *Neuroscience Letters*, *163*(1).

Nauta, W. J. (1972). Neural associations of the frontal cortex. *Acta Neurobiologiae Experimentalis*, *32*(2), 125–140. http://www.ncbi.nlm.nih.gov/pubmed/4627612

Noudoost, B., Clark, K. L., & Moore, T. (2021). Working memory gates visual input to primate prefrontal neurons. *ELife*, *10*. https://doi.org/10.7554/ELIFE.64814

Perez-Cruz, C., Simon, M., Flügge, G., Fuchs, E., & Czéh, B. (2009). Diurnal rhythm and stress regulate dendritic architecture and spine density of pyramidal neurons in the rat infralimbic cortex. *Behavioural Brain Research*, *205*(2), 406–413. https://doi.org/10.1016/j.bbr.2009.07.021

Provencio, I., & Warthen. (2012). The role of intrinsically photosensitive retinal ganglion cells in nonimage-forming responses to light. *Eye and Brain*, *4*, 43. https://doi.org/10.2147/eb.s27839

Quattrochi, L. E., Stabio, M. E., Kim, I., Ilardi, M. C., Michelle Fogerson, P., Leyrer, M. L., & Berson, D. M. (2019). The M6 cell: A small-field bistratified photosensitive retinal ganglion cell. *Journal of Comparative Neurology*, *527*(1), 297–311. https://doi.org/10.1002/cne.24556

Salay, L. D., Ishiko, N., & Huberman, A. D. (2018). A midline thalamic circuit determines reactions to visual threat. *Nature*, *557*(7704), 183–189. https://doi.org/10.1038/s41586-018-0078-2

SATO, M. (1971). Prefrontal Cortex and Emotional Behaviors. *Psychiatry and Clinical Neurosciences*, *25*(1), 69–78. https://doi.org/10.1111/j.1440-1819.1971.tb01489.x

Saunders, A., Macosko, E. Z., Wysoker, A., Brumbaugh, S., Kulp, D., Mccarroll, S. A., Saunders, A., Macosko, E. Z., Wysoker, A., Goldman, M., & Krienen, F. M. (2018). Molecular Diversity and Specializations among the Cells of the Adult Mouse Brain Resource Molecular Diversity and

Specializations among the Cells of the Adult Mouse Brain. *Cell*, *174*(4), 1015-1030.e16. https://doi.org/10.1016/j.cell.2018.07.028

Saxena, A., Wagatsuma, A., Noro, Y., Kuji, T., Asaka-Oba, A., Watahiki, A., Gurnot, C., Fagiolini, M., Hensch, T. K., & Carninci, P. (2012). Trehalose-enhanced isolation of neuronal sub-types from adult mouse brain. *BioTechniques*, *52*(6), 381–385. https://doi.org/10.2144/0000113878

Stuart, T., Butler, A., Hoffman, P., Hafemeister, C., Papalexi, E., Mauck, W. M., Hao, Y., Stoeckius, M., Smibert, P., & Satija, R. (2019). Comprehensive Integration of Single-Cell Data. *Cell*, *177*(7), 1888-1902.e21. https://doi.org/10.1016/j.cell.2019.05.031

Takahashi, A., Nagayasu, K., Nishitani, N., Kaneko, S., & Koide, T. (2014). Control of Intermale Aggression by Medial Prefrontal Cortex Activation in the Mouse. *PLoS ONE*, *9*(4), e94657. https://doi.org/10.1371/journal.pone.0094657

Uylings, H. B. M., & Van Eden, C. G. (1991). Chapter 3 Qualitative and quantitative comparison of the prefrontal cortex in rat and in primates, including humans. *Progress in Brain Research*, *85*(C), 31–62. https://doi.org/10.1016/S0079-6123(08)62675-8

Vertes, R. P. (2004). Differential projections of the infralimbic and prelimbic cortex in the rat. *Synapse (New York, N.Y.)*, *51*(1), 32–58. https://doi.org/10.1002/SYN.10279

Zeisel, A., Hochgerner, H., Ernfors, P., Lo, P., Marklund, U., Linnarsson, S., Johnsson, A., Memic, F., & Zwan, J. Van Der. (2018). *Resource Molecular Architecture of the Mouse Nervous System*. 999–1014. https://doi.org/10.1016/j.cell.2018.06.021

Zhou, Y., Zhang, H. K., Liu, F., Lei, G., Liu, P., Jiao, T., & Dang, Y. H. (2018). Altered Light Conditions Contribute to Abnormalities in Emotion and Cognition Through HINT1 Dysfunction in C57BL/6 Mice. *Frontiers in Behavioral Neuroscience*, *12*. https://doi.org/10.3389/FNBEH.2018.00110

Bachevalier, J., & Loveland, K. A. (2006). The orbitofrontal-amygdala circuit and self-regulation of social-emotional behavior in autism. *Neuroscience and Biobehavioral Reviews*, *30*(1), 97–117. https://doi.org/10.1016/j.neubiorev.2005.07.002

Berson, D.M., Dunn, F.A., Takao, M. (2002). Phototransduction by retinal ganglion cells that set the circadian clock. *Science*, 295(5557):1070-3. doi: 10.1126/science.1067262.

Bianchi, L. (1922). The Mechanism of the Brain and the Function of the Frontal Lobes. *Journal of Mental Science, 68(283), Quoted in Fuster, J. (2015), "The Prefrontal Cortex", 5th Edition.*

Bicks, L. K., Koike, H., Akbarian, S., & Morishita, H. (2015). Prefrontal Cortex and Social Cognition in Mouse and Man. *Frontiers in Psychology*, *6*, 1805. https://doi.org/10.3389/fpsyg.2015.01805

Bloodgood, B. L., Sharma, N., Browne, H. A., Trepman, A. Z., & Greenberg, M. E. (2013). The activity-dependent transcription factor NPAS4 regulates domain-specific inhibition. *Nature*, *503*(7474), 121–125. https://doi.org/10.1038/nature12743

Brodmann, K. (1912). Neue Ergebnisse über die vergleichende histologische Lokalisation der Grosshirnrinde mit besonderer Berücksichtigung. *Anat. Anzeiger. 41, 157-216. Quoted in Fuster, J. (2015). "The Prefrontal Cortex", 5th Edition.*

BRODY, E. B., & ROXVOLD, H. E. (1952). Influence of prefrontal lobotomy on social interaction in a monkey group. *Psychosomatic Medicine*, *14*(5), 406–415. https://doi.org/10.1097/00006842-195209000-00007

Carrington, S. J., & Bailey, A. J. (2009). Are there theory of mind regions in the brain? A review of the neuroimaging literature. In *Human Brain Mapping* (Vol. 30, Issue 8, pp. 2313–2335). https://doi.org/10.1002/hbm.20671

Chen, S.-K., Badea, T. C., & Hattar, S. (2011). Photoentrainment and pupillary light reflex are mediated by distinct populations of ipRGCs. *Nature*, *476*(7358), 92–95. https://doi.org/10.1038/nature10206

Chew, K.S., Renna, J.M., McNeill, D.S., Fernandez, D.C., Keenan, W.T., Thomsen, M.B., Ecker, J.L., Loevinsohn, G.S., VanDunk, C., Vicarel, D.C., Tufford, A., Weng, S., Gray, P.A., Cayouette, M., Herzog, E.D., Zhao, H., Berson, D.M., Hattar, S. (2017). A subset of ipRGCs regulates both maturation of the circadian clock and segregation of retinogeniculate projections in mice. *eLife*, pii: e22861. doi: 10.7554/eLife.22861.

De Boer, S., & Koolhaas, J. (2003). Defensive burying in rodents: ethology, neurobiology and psychopharmacology. *European Journal of Pharmacology*, *463*(1–3).

De Bruin, J. P. C., Van Oyen, H. G. M., & Van De Poll, N. (1983). Behavioural changes following lesions of the orbital prefrontal cortex in male rats. *Behavioural Brain Research*, *10*(2–3), 209–232. https://doi.org/10.1016/0166-4328(83)90032-3

Ecker, J. L., Dumitrescu, O. N., Wong, K. Y., Alam, N. M., Chen, S.-K., LeGates, T., Renna, J. M., Prusky, G. T., Berson, D. M., & Hattar, S. (2010). Melanopsin-Expressing Retinal Ganglion-Cell Photoreceptors: Cellular Diversity and Role in Pattern Vision. *Neuron*, *67*(1), 49–60. https://doi.org/10.1016/j.neuron.2010.05.023

Ellegood, J., & Crawley J. N. (2015) Behavioral and Neuroanatomical Phenotypes in Mouse Models of Autism. *Neurotherapeutics*, vol 12, pp. 521-533.

Fernandez, D. C., Fogerson, P. M., Lazzerini Ospri, L., Thomsen, M. B., Layne, R. M., Severin, D., Zhan, J., Singer, J. H., Kirkwood, A., Zhao, H., Berson, D. M., & Hattar, S. (2018). Light Affects Mood and Learning through Distinct Retina-Brain Pathways. *Cell*, *175*(1), 71-84.e18.

https://doi.org/10.1016/j.cell.2018.08.004

Franklin, K.B.J, & Chudasama, Y. (2012). Prefrontal Cortex. In The mouse Nervous System. C. Watson, G. Paxinos & L. Puelles. (Elsevier Inc.). pp. 727-735.

Franzen, E. A., & Myers, R. E. (1973). Neural control of social behavior: prefrontal and anterior temporal cortex. *Neuropsychologia*, *11*(2), 141–157. https://doi.org/10.1016/0028-3932(73)90002-x

Fuster, J. (2001). The Prefrontal Cortex—An Update. *Neuron*, *30*(2).

Gianfranceschi, L., Siciliano, R., Walls, J., Morales, B., Kirkwood, A., Huang, Z.J., Tonegawa, S., & Maffei, L. (2003). Visual cortex is rescued from the effects of dark rearing by overexpression of BDNF. *PNAS*, 100 (21) 12486-12491; https://doi.org/10.1073/pnas.1934836100

Güler, A. D., Ecker, J. L., Lall, G. S., Haq, S., Altimus, C. M., Liao, H.-W., Barnard, A. R., Cahill, H., Badea, T. C., Zhao, H., Hankins, M. W., Berson, D. M., Lucas, R. J., Yau, K.-W., & Hattar, S. (2008). Melanopsin cells are the principal conduits for rod–cone input to non-image-forming vision. *Nature*, *453*(7191), 102–105. https://doi.org/10.1038/nature06829

Hattar, S., Liao, H.W., Takao, M., Berson, D.M., & Yau, K.-W. (2002). Melanopsin-containing retinal ganglion cells: architecture, projections, and intrinsic photosensitivity. *Science*, 295(5557):1065-70. doi: 10.1126/science.1069609.

Heisler, J. M., Morales, J., Donegan, J. J., Jett, J. D., Redus, L., & O'connor, J. C. (2015). The attentional set shifting task: A measure of cognitive flexibility in mice. *Journal of Visualized Experiments*, *96*. https://doi.org/10.3791/51944

Hiser, J., & Koenigs, M. (2018). The Multifaceted Role of the Ventromedial Prefrontal Cortex in Emotion, Decision Making, Social Cognition, and Psychopathology. *Biological Psychiatry*, *83*, 638–647. https://doi.org/10.1016/j.biopsych.2017.10.030

Huang, D. W., Sherman, B. T., & Lempicki, R. A. (2009). Systematic and integrative analysis of large gene lists using DAVID bioinformatics resources. *Nature Protocols*, *4*(1), 44–57. https://doi.org/10.1038/nprot.2008.211

Izquierdo, A., Wellman, C. L., & Holmes, A. (2006). Brief Uncontrollable Stress Causes Dendritic Retraction in Infralimbic Cortex and Resistance to Fear Extinction in Mice. *Journal of Neuroscience*, *26*(21), 5733–5738. https://doi.org/10.1523/JNEUROSCI.0474-06.2006

Koechlin, E., Ody, C., & Kouneiher, F. (2003). The Architecture of Cognitive Control in the Human Prefrontal Cortex. *Science*, *302*(5648), 1181–1185. https://doi.org/10.1126/science.1088545

Lazzerini Ospri, L., Prusky, G., & Hattar, S. (2017). Mood, the Circadian System, and Melanopsin Retinal Ganglion Cells. *Annual Review of Neuroscience*, *40*(1), annurev-neuro-072116-031324.

https://doi.org/10.1146/annurev-neuro-072116-031324

LeGates, T. A., Altimus, C. M., Wang, H., Lee, H.-K., Yang, S., Zhao, H., Kirkwood, A., Weber, E. T., & Hattar, S. (2012). Aberrant light directly impairs mood and learning through melanopsin-expressing neurons. *Nature*, *491*(7425), 594–598. https://doi.org/10.1038/nature11673

McClung, C., Burns, J., Parekh, P., & Dzirasa, K. (2018). 161. The Clock Protein Regulates Neuronal Maturation and Function in the mPFC. *Biological Psychiatry*, *83*(9), S65–S66. https://doi.org/10.1016/j.biopsych.2018.02.179

Morgan, M., Romanski, L., & LeDoux, J. (1993). Extinction of emotional learning: contribution of medial prefrontal cortex. *Neuroscience Letters*, *163*(1).

Nauta, W. J. (1972). Neural associations of the frontal cortex. *Acta Neurobiologiae Experimentalis*, *32*(2), 125–140. http://www.ncbi.nlm.nih.gov/pubmed/4627612

Perez-Cruz, C., Simon, M., Flügge, G., Fuchs, E., & Czéh, B. (2009). Diurnal rhythm and stress regulate dendritic architecture and spine density of pyramidal neurons in the rat infralimbic cortex. *Behavioural Brain Research*, *205*(2), 406–413. https://doi.org/10.1016/j.bbr.2009.07.021

Provencio, I., Rodriguez, I.R., Jiang, G., Hayes, W.P., Moreira, E.F., Rollag, M.D. (2000). A novel human opsin in the inner retina. *J Neurosci*, 20(2):600-5. doi: 10.1523/JNEUROSCI.20-02-00600.2000.

Provencio, I., & Warthen. (2012). The role of intrinsically photosensitive retinal ganglion cells in nonimage-forming responses to light. *Eye and Brain*, *4*, 43. https://doi.org/10.2147/eb.s27839

Quattrochi, L. E., Stabio, M. E., Kim, I., Ilardi, M. C., Michelle Fogerson, P., Leyrer, M. L., & Berson, D. M. (2019). The M6 cell: A small-field bistratified photosensitive retinal ganglion cell. *Journal of Comparative Neurology*, *527*(1), 297–311. https://doi.org/10.1002/cne.24556

Salay, L. D., Ishiko, N., & Huberman, A. D. (2018). A midline thalamic circuit determines reactions to visual threat. *Nature*, *557*(7704), 183–189. https://doi.org/10.1038/s41586-018-0078-2

SATO, M. (1971). Prefrontal Cortex and Emotional Behaviors. *Psychiatry and Clinical Neurosciences*, *25*(1), 69–78. https://doi.org/10.1111/j.1440-1819.1971.tb01489.x

Saunders, A., Macosko, E. Z., Wysoker, A., Brumbaugh, S., Kulp, D., Mccarroll, S. A., Saunders, A., Macosko, E. Z., Wysoker, A., Goldman, M., & Krienen, F. M. (2018). Molecular Diversity and Specializations among the Cells of the Adult Mouse Brain Resource Molecular Diversity and Specializations among the Cells of the Adult Mouse Brain. *Cell*, *174*(4), 1015-1030.e16. https://doi.org/10.1016/j.cell.2018.07.028

Saxena, A., Wagatsuma, A., Noro, Y., Kuji, T., Asaka-Oba, A., Watahiki, A., Gurnot, C., Fagiolini, M., Hensch, T. K., & Carninci, P. (2012). Trehalose-enhanced isolation of neuronal sub-types from

adult mouse brain. *BioTechniques*, *52*(6), 381–385. https://doi.org/10.2144/0000113878

Schmidt, T.M., Alam, N.M., Chen, S., Kofuji, P., Li, W., Prusky, G.T., Hattar, S. (2014). A role for melanopsin in alpha retinal ganglion cells and contrast detection. *Neuron*, 82(4):781-8. doi: 10.1016/j.neuron.2014.03.022.

Stone, V. E., Baron-Cohen, S., & Knight, R. T. (1998). Frontal lobe contributions to theory of mind. *Journal of Cognitive Neuroscience*, *10*(5), 640–656. https://doi.org/10.1162/089892998562942

Stuart, T., Butler, A., Hoffman, P., Hafemeister, C., Papalexi, E., Mauck, W. M., Hao, Y., Stoeckius, M., Smibert, P., & Satija, R. (2019). Comprehensive Integration of Single-Cell Data. *Cell*, *177*(7), 1888-1902.e21. https://doi.org/10.1016/j.cell.2019.05.031

Takahashi, A., Nagayasu, K., Nishitani, N., Kaneko, S., & Koide, T. (2014). Control of Intermale Aggression by Medial Prefrontal Cortex Activation in the Mouse. *PLoS ONE*, *9*(4), e94657. https://doi.org/10.1371/journal.pone.0094657

Uylings, H. B. M., & Van Eden, C. G. (1991). Chapter 3 Qualitative and quantitative comparison of the prefrontal cortex in rat and in primates, including humans. *Progress in Brain Research*, *85*(C), 31–62. https://doi.org/10.1016/S0079-6123(08)62675-8

Zeisel, A., Hochgerner, H., Ernfors, P., Lo, P., Marklund, U., Linnarsson, S., Johnsson, A., Memic, F., & Zwan, J. Van Der. (2018). *Resource Molecular Architecture of the Mouse Nervous System*. 999–1014. https://doi.org/10.1016/j.cell.2018.06.021

Figure Legends

Figure 1. Loss of ipRGCs leads to apical dendritic degeneration in the vmPFC. We reconstructed the apical dendritic trees of pyramidal neurons in layer III-, throughout the anterio-posterior extension of the IL and PL areas (+1.9 to +1.3 mm relative to bregma), from Golgi-stained coronal sections. **A.** Sholl analysis revealed a significant degeneration of both proximal branches and distal tufts in animals (littermate controls) conceived and reared in constant darkness (DD), and ipRGC-ablated animals (specifically, Brn3bDTA) ($p<0.001$, repeated-measures ANOVA). **B.** The total apical dendritic length is significantly ($p<0.001$) reduced in DD mice (849.37±43.13) relative to LD controls (1327.89±36.22). **C.** The number of branch nodes was also significantly reduced ($p<0.001$) in DD mice (9.70±0.68) relative to LD controls (17.39±0.46). **D.** Sholl analysis revealed a significant degeneration of both proximal branches and distal tufts in LD littermate controls (Cntrl) relative to aDTA and Brn3bDTA animals ($p<0.001$, repeated-measures ANOVA). **E.** In aDTA mice, at 7 weeks of age (light red), apical dendrites had a wildtype morphology, significantly different than at 6 months (dark red, re-plotted from

C)(p<0.001, repeated-measures ANOVA). **F.** Dramatic examples of apical dendritic shrinkage; compare neurons from wild-type (leftmost) and young (7 week old) aDTA mice (center-left) with affected neurons in old (>6 month old) aDTA (center-right) and brn3bDTA mice (rightmost). **G.** The total apical dendritic length was not significantly different between controls (1360.06±85.18) and aDTAs (1374.83±94.25) at 7 weeks of age; **H.** it is still not significantly different at 3 to 4 months of age (controls 1327±36.22 vs. aDTAs 1196.33±104.34); **I.** it becomes significantly different (p<0.0001) at older than 6 months (controls 1358.62±31.28 vs. aDTAs 950.07±48.60); the same significant difference is observed in age-matched Brn3bDTAs (894.12±81.77). **J.** This panel replots data from aDTAs pre- and post- ipRGC degeneration for between-ages comparison within this genotype (p<0.001)(t-test). **K.** The number of branch points was not significantly different between controls and aDTAs at 7 weeks of age (14.19±1.04 vs. 14.58±0.97 respectively); **L.** an incipient significant difference was observed at 3 to 4 months (17.39±0.46 vs. 11.68±0.94, p<0.001); **M.** which increased at older ages than 6 months (16.14±0.63 vs. 10.39±0.59, p<0.001); **N.** There is a significant difference within the aDTA genotype between 7 weeks and over 6 months of age (p<0.001)(t-test). All values are mean±SEM. In the plots, each dot represents one animal.

Figure 2. vmPFC activity in response to a stressful stimulus is depressed in ipRGC-ablated mice. **A.** Neurons were transduced with GCaMP6f; an optical fiber was implanted above the area. **B.** Mice were exposed to a loud sound—a non-visual fear-evoking stimulus. **C.** We recorded in vivo neuronal activity from the vmPFC. Recordings of endogenous activity showed a significantly higher number of peaks in controls relative to Brn3bDTAs at ZT12 (p=0.037), ZT18 (p=0.028), and ZT6 (p=0.002). A trend in the same direction is present at ZT0 (p=0.116). All values are mean±SEM. **D.** Examples to highlight high intrinsic activity recording from a control mouse (top) vs. a low intrinsic activity trace from a Brn3bDTA (bottom). **Traces are individual recordings; the thicker line is a rolling time average. E.** Normalized Ca^{2+}-dependent fluorescence in response to the noise (delivered at time=0) in controls (left) and Brn3bDTA mice (right). Traces are mean (±SEM, hued area) of recordings from 3 animals, each averaged over multiple trials. **F.** Fluorescence decayed to baseline more slowly in controls than in ipRGC-ablated mutants (22.08±5.85 s vs. 4.13±0.92 s)(p=0.039). **G.** The Area Under the Curve of vmPFC activity in response to this stimulus was significantly higher in controls (0.204±0.0230) vs. ipRGC-ablated mice (0.030±0.0048)(p=0.002).

Figure 3. Genes associated with neurotransmission and synaptic plasticity are severely dysregulated in the vmPFC of ipRGC-ablated mice. **A.** UMAP plot of all neurons identified in the vmPFC. **B.** Same as

in A overlaid with sample genotype. **C.** Same as in A overlaid with major neuron type assignment. **D.** Relative neuron cluster composition by genotype (red=DTA, blue=control). **E.** Relative expression of the most significantly differentially-expressed genes in DTA cells across all clusters. **F.** Volcano plot of differentially expressed genes between DTA and control samples within unspecified neuronal cluster U1. **G-H.** Gene ontology terms significantly enriched in the downregulated (G) or upregulated (H) genes from (F).

Figure 4. ipRGC-ablated mice show impaired regulation of emotion and attention. **A.** In a free-interaction assay, a test mouse is exposed to a strange conspecific in an unfamiliar arena. **B.** ipRGC-ablated mice were less likely to interact socially, spending 30.85±5.07% of their time in this activity vs. 51.4±6.44% for controls (p=0.025). **C.** The reason for decreased social interaction time was increased distancing. **D.** In the looming test, a mouse can react to a simulated predator by running under a shelter, freezing and/or rattling his tail. The last is a known mPFC-dependent behavior. **E.** A similar proportion of ipRGC-ablated mice ran under the shelter and froze relative to littermate controls (sheltering: 73.33% vs. 85.71%; freezing: 40% vs. 50%), but they were less likely to rattle their tails (20% vs. 57.14%, p=0.027) (Normal Approximation proportion test). The plot shows what proportion of specified behavior was displayed by control vs. ipRGC-ablated mice (normalized). **F.** In the defensive burying test, mice bury a fox-urine-soaked Q-tip if they can overcome their fear of the scent. **G.** ipRGC-ablated mice were less likely to bury the noxious object: 40% did (dark red), vs. 80% of littermate controls (dark blue), p=0.025) (Normal Approximation proportion test). **H.** Restricting the analysis to those that dared to bury it, a difference was also evident in the latency to enact this behavior (647±147.4 s for ipRGC-ablated mice vs. 271.1±66.2 s for controls, p=0.015). **I.** The Attention Set Shift Test is a task in which cognitive flexibility and attention interact with emotional drives. **J.** We recorded the latency necessary for a mouse to enact a correction for an initial incorrect choice after a reward-association rule was learned. For each stage of the test, the p-value of the performance difference between genotypes is reported over the bars. ipRGC-ablated mice took longer to enact corrective behavior in the EDS (10.61±1.32 s vs. 6.9±0.44 s, p=0.023). In the plots, each dot represents one animal.

Supplementary Figure 1. A. The motor cortex, a control region, is unaffected. **B.** Sholl analysis consists in counting the number of intersections between a dendritic tree and concentric circles of increasing radius centered on the soma. **C.** Neurons in the motor cortex of control and ipRGC-ablated mice do not display morphological difference.

Supplementary Figure 2. RNAseq from the vmPFC. **A.** Outline of experimental setup. **B.** UMAP plot of 24,340 single cells isolated from the adult vmPFC, colored by major cell type identification. **C.** Same as in B. overlaid with sample genotype. **D.** Marker genes used for major cell type assignments.

Supplementary Figure 3. Neuronal identification in vmPFC. **A.** Dot plot of marker genes for all identified excitatory neuron populations. **B.** ISH images from the Allen Brain Atlas showing the physical expression patterns of major genes identified in B. **C.** Dot plot of marker genes for all identified inhibitory neurons. **D.** ISH images from the Allen Brain Atlas showing physical expression patterns of genes identified in D.

Supplementary Figure 4. RNAseq from the motor cortex. **A.** UMAP plot of all cells collected from the mouse motor cortex (control: 6229, DTA: 2373). **B.** Same as in A overlaid with sample genotype.

Supplementary Figure 5. A. In a 3-chamber test a mouse has to choose whether to spend time in a chamber with a caged conspecific or in another chamber with an object. **B.** During the first two minutes of the test, ipRGC-ablated mice displayed decreased social-chamber time ($p=0.014$). **C.** Individual paths and averaged heatmaps of mice in the 3-chamber test. **D.** In the attention set shift test, ipRGC-ablated mice surprisingly demonstrated an impaired rule-learning ability in the IDS2, which is the first stage tested during the second day of the test. They required significantly more trials to learn the reward-association rule (19.9±1.49 vs. 12.25±2.07, $p=0.007$).

Supplementary Figure 6. A. The number of fights initiated by test mice in the Reciprocal Interaction Test was not different between genotypes, and neither was the time spent immobile. **B.** Without prior social isolation there was no significant difference between genotypes in social contact (although a trend exists). **C.** The marble burying test assesses anxiety elicited by a novel environment. ipRGC-ablated mice did not differ in this behavior from littermate controls (6.4±1.7 marbles buried vs. 6.2±1.1, $p=0.93$). **D.** A mouse approaches an object soaked with a chemical (TMT) giving fox urine its characteristic odor (from the defensive burying test described in Fig. 4F). **E. In the Attention Set Shift Test, ipRGC-ablated mice were significantly impaired in learning the association rule in IDS2. This may suggest dysregulation in additional prefrontal areas, possibly as a secondary effect from the vmPFC alterations.**

Supplementary Figure S7. Validation of Differentially Expressed Genes Identified by Single-Cell RNA Sequencing Using RNAScope. (A)-(B) In (A), a schematic diagram is presented, outlining the specific brain region selected for both representative images and subsequent quantification, as highlighted by the red boxes. In (B), a representative DAPI staining image of this brain area is shown. (C)-(F) In these panels, you can observe representative RNAscope images obtained from control mice (on the left) and DTA mice (in the middle). The corresponding quantification results are displayed on the right, illustrating the analysis for the following markers: (C) map2, (D) nlgn2, (E) gls, and (F) ubb. The statistical analysis was carried out using an unpaired Student's t-test, with data collected from 2-3 mice and 4-6 sections in each case.
The data is presented as means ± SEM, with significance levels indicated as follows: *P < 0.05; ***P < 0.001.

Supplementary Figure S8. Validation of Differentially Expressed Genes Identified by Single-Cell RNA Sequencing Using RNAScope. (A)-(B) This figure displays a schematic diagram (A) and a representative DAPI staining image (B) that visually convey the brain region specifically chosen for the presentation of illustrative images and subsequent quantification in panels (C)-(F), as indicated by the presence of red boxes.
(C)-(F) In these panels, you can observe representative RNAscope images obtained from control mice (on the left) and DTA mice (in the middle). The quantification results, shown on the right, pertain to the analysis of the following markers: (C) cntnap2, (D) pfn2, (E) hspa8, and (F) gad2. The statistical analysis employed an unpaired Student's t-test, with data collected from 2-3 mice and 4-6 sections for each group.
Data is depicted as means ± SEM, and "ns" designates non-significant differences.

Supplementary Video 1. *Free Interaction test of Brn3DTA mouse*. Mouse is in cage for 1 minute. At ~1 minute a wildtype mouse is introduced. Total length is ~9mins.

Supplementary Video 2. *Three Chamber test*. A control mouse explores the left side of the three chambers, where a mouse is located. In the right side of the three chambers, an object is provided. Total length is ~2mins.

Supplementary Video 3. *Three Chamber test*. A Brn3DTA mouse avoids the left side of the three chambers, where a mouse is located. In the right side of the three chambers, an object is provided. Total length is ~2mins.

Supplementary Video 4. *Tail rattling in the looming test*. A Brn3DTA mouse rattles his tail in response to a looming stimulus. Total length is less than half a minute.

Supplementary Video 5. *Defensive burying test*. At ~10 seconds, the fox urine is introduced to the cage. Note how the Brn3bDTA mouse avoids the scent and only tries to bury it ~3mins into the video. Total length is ~6mins

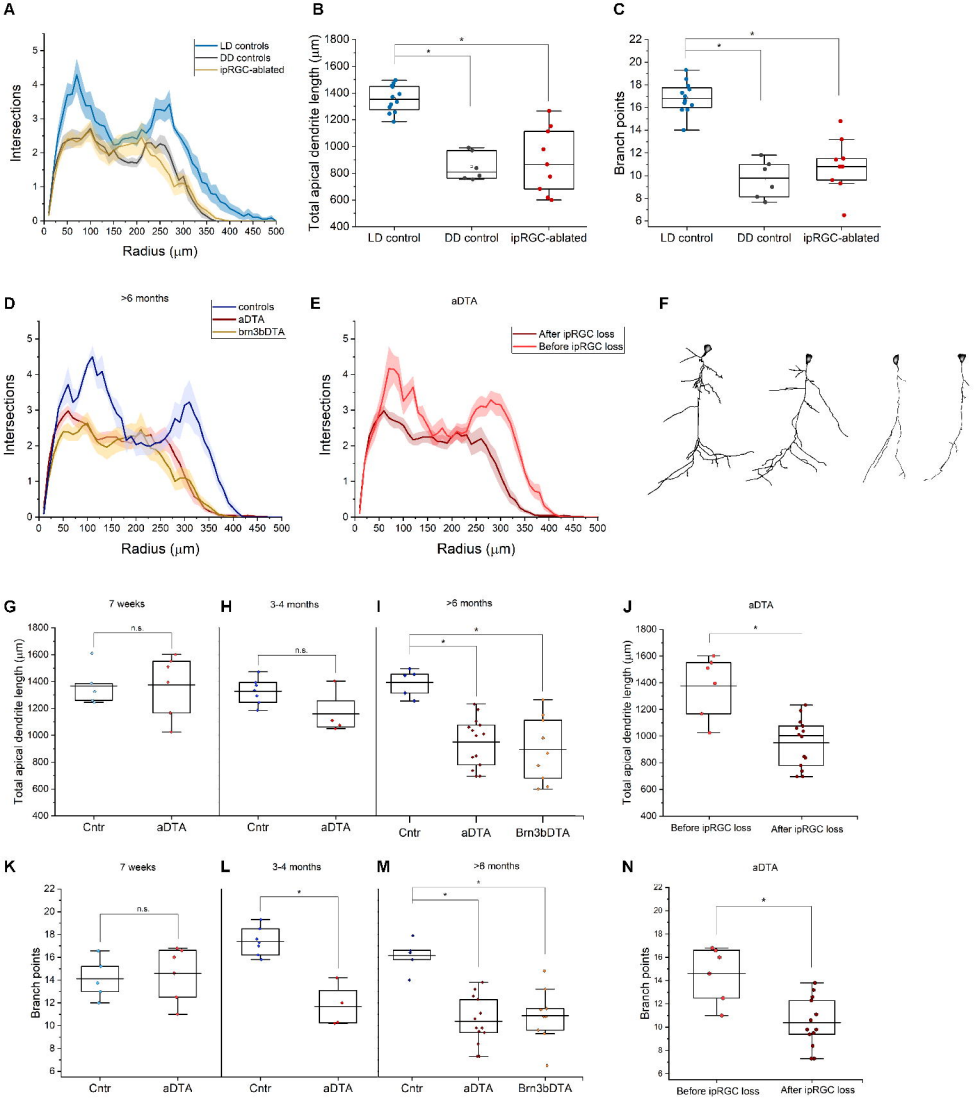
A
LD controls
DD controls
ipRGC-ablated
Intersections
Radius (μm)
B
Total apical dendrite length (μm)
LD control
DD control
ipRGC-ablated
C
Branch points
LD control
DD control
ipRGC-ablated
D
>6 months
controls
aDTA
brn3bDTA
Intersections
Radius (μm)
E
aDTA
After ipRGC loss
Before ipRGC loss
Intersections
Radius (μm)
F
G
7 weeks
n.s.
Total apical dendrite length (μm)
Cntr
aDTA
H
3-4 months
n.s.
Cntr
aDTA
I
>6 months
Cntr
aDTA
Brn3bDTA
J
aDTA
Total apical dendrite length (μm)
Before ipRGC loss
After ipRGC loss
K
7 weeks
n.s.
Branch points
Cntr
aDTA
L
3-4 months
Cntr
aDTA
M
>6 months
Cntr
aDTA
Brn3bDTA
N
aDTA
Branch points
Before ipRGC loss
After ipRGC loss

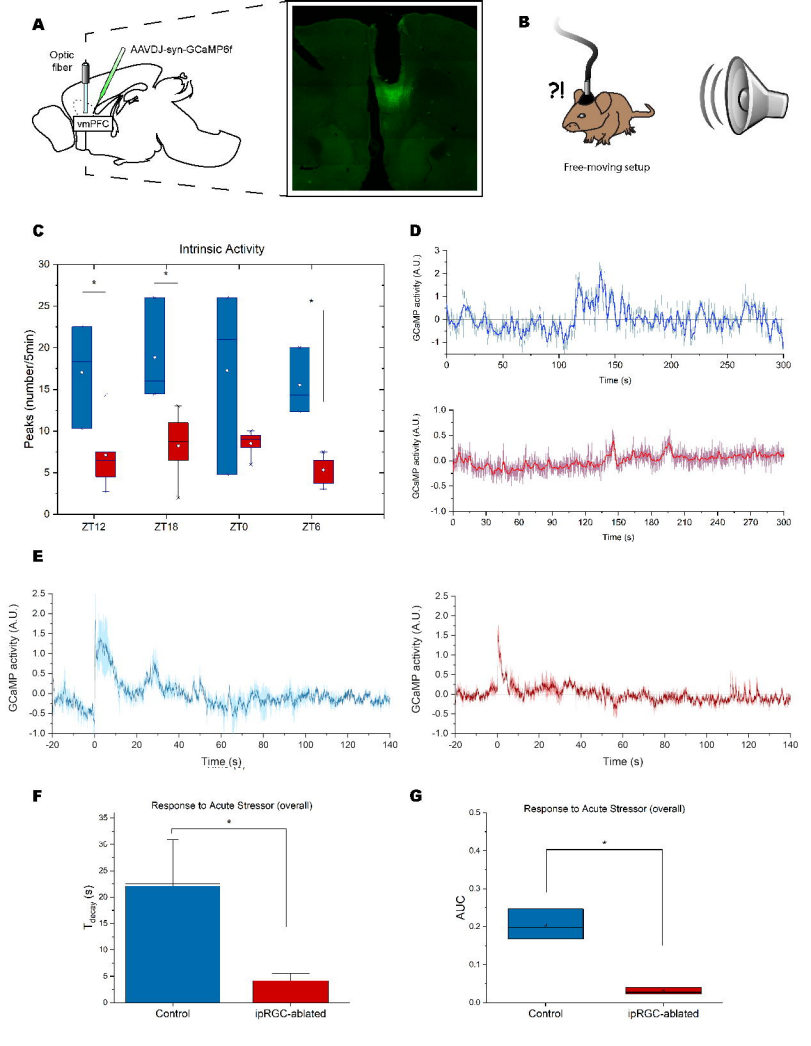
A
Optic fiber
AAVDJ-syn-GCaMP6f
vmPFC
B
?!
Free-moving setup
C
Intrinsic Activity
Peaks (number/5min)
ZT12
ZT18
ZT0
ZT6
D
GCaMP activity (A.U.)
Time (s)
E
GCaMP activity (A.U.)
Time (s)
F
Response to Acute Stressor (overall)
T_{decay} (s)
Control
ipRGC-ablated
G
Response to Acute Stressor (overall)
AUC
Control
ipRGC-ablated

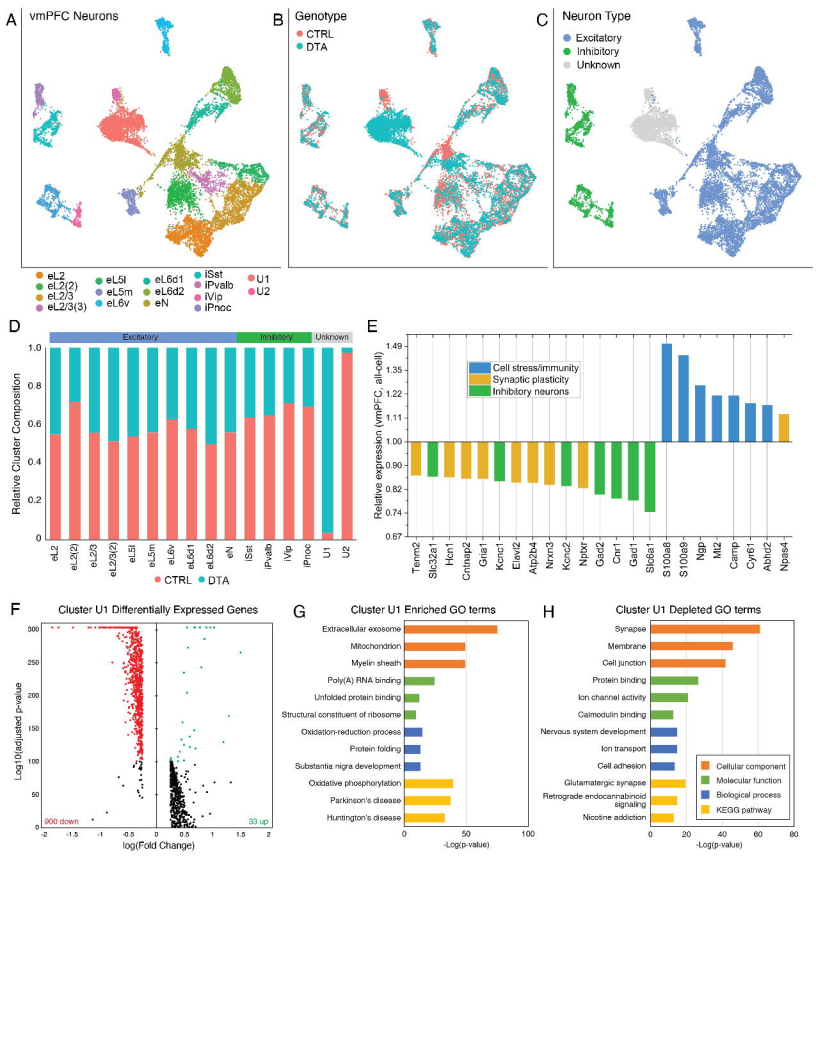
A
vmPFC Neurons
B
Genotype
CTRL
DTA
C
Neuron Type
Excitatory
Inhibitory
Unknown
eL2
eL2(2)
eL2/3
eL2/3(3)
eL5I
eL5m
eL6v
eL6d1
eL6d2
eN
iSst
iPvalb
iVip
iPnoc
U1
U2
D
Excitatory
Inhibitory
Unknown
Relative Cluster Composition
CTRL
DTA
E
Cell stress/immunity
Synaptic plasticity
Inhibitory neurons
Relative expression (vmPFC: all-cell)
Tenm2
Slc32a1
Hcn1
Cntnap2
Gria1
Kcnc1
Elavl2
Atp2b4
Nrxn3
Kcnc2
Nptxr
Gad2
Cnr1
Gad1
Slc6a1
S100a8
S100a9
Ngp
Mt2
Camp
Cyr61
Atbhd2
Ngas4
F
Cluster U1 Differentially Expressed Genes
Log10(adjusted p-value)
900 down
33 up
log(Fold Change)
G
Cluster U1 Enriched GO terms
Extracellular exosome
Mitochondrion
Myelin sheath
Poly(A) RNA binding
Unfolded protein binding
Structural constituent of ribosome
Oxidation-reduction process
Protein folding
Substantia nigra development
Oxidative phosphorylation
Parkinson's disease
Huntington's disease
-Log(p-value)
H
Cluster U1 Depleted GO terms
Synapse
Membrane
Cell junction
Protein binding
Ion channel activity
Calmodulin binding
Nervous system development
Ion transport
Cell adhesion
Glutamatergic synapse
Retrograde endocannabinoid signaling
Nicotine addiction
Cellular component
Molecular function
Biological process
KEGG pathway
-Log(p-value)

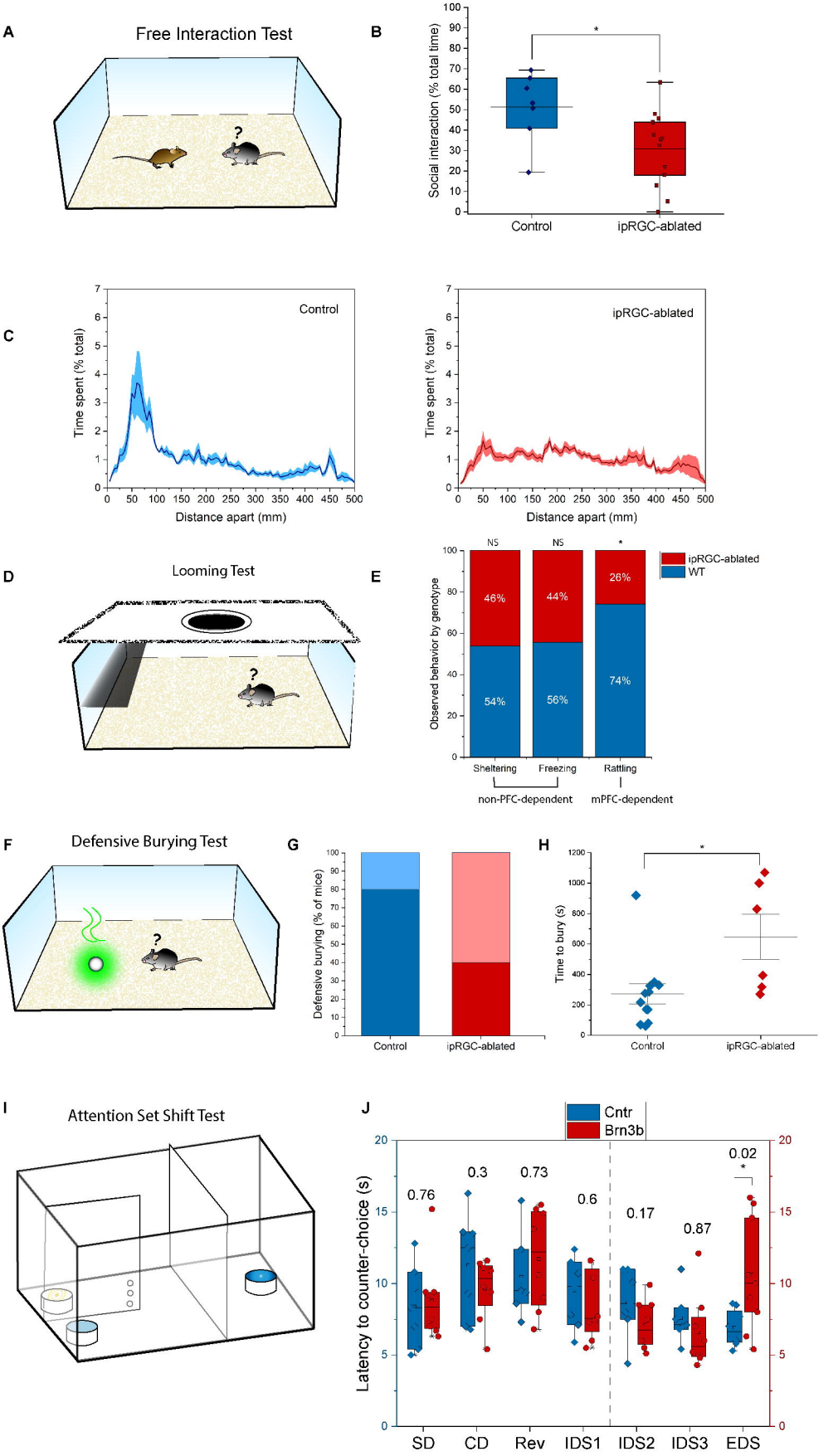
A
Free Interaction Test
B
Social interaction (% total time)
Control
ipRGC-ablated
C
Control
ipRGC-ablated
Time spent (% total)
Distance apart (mm)
D
Looming Test
E
NS
NS
*
ipRGC-ablated
WT
46%
44%
26%
54%
56%
74%
Observed behavior by genotype
Sheltering
Freezing
Rattling
non-PFC-dependent
mPFC-dependent
F
Defensive Burying Test
G
Defensive burying (% of mice)
Control
ipRGC-ablated
H
Time to bury (s)
Control
ipRGC-ablated
I
Attention Set Shift Test
J
Cntr
Brn3b
Latency to counter-choice (s)
0.76
0.3
0.73
0.6
0.17
0.87
0.02
SD
CD
Rev
IDS1
IDS2
IDS3
EDS

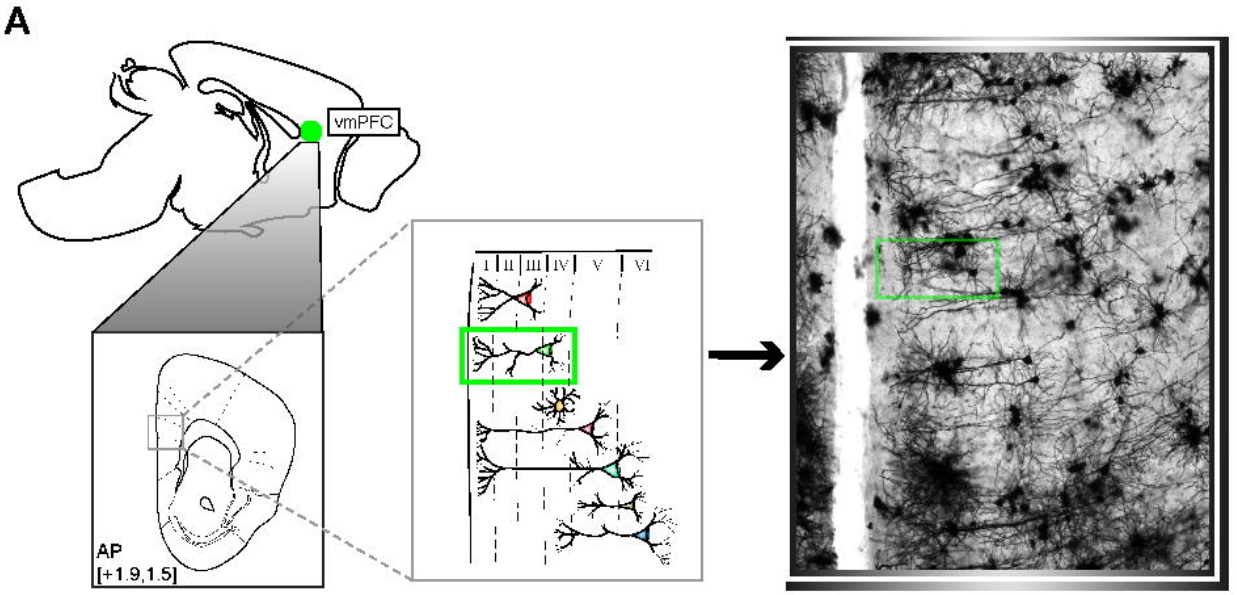
A
vmPFC
AP
[+1.9,1.5]
I
II
III
IV
V
VI

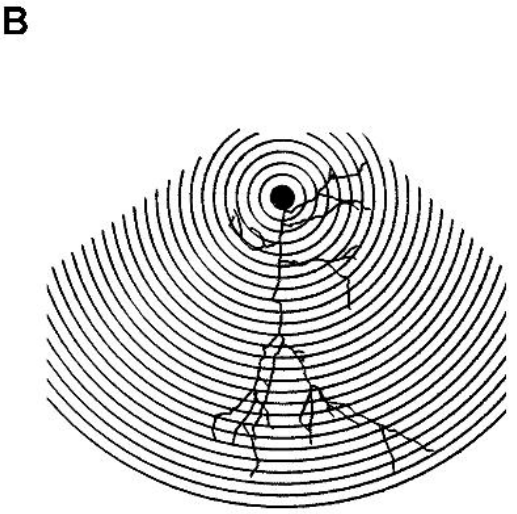
B

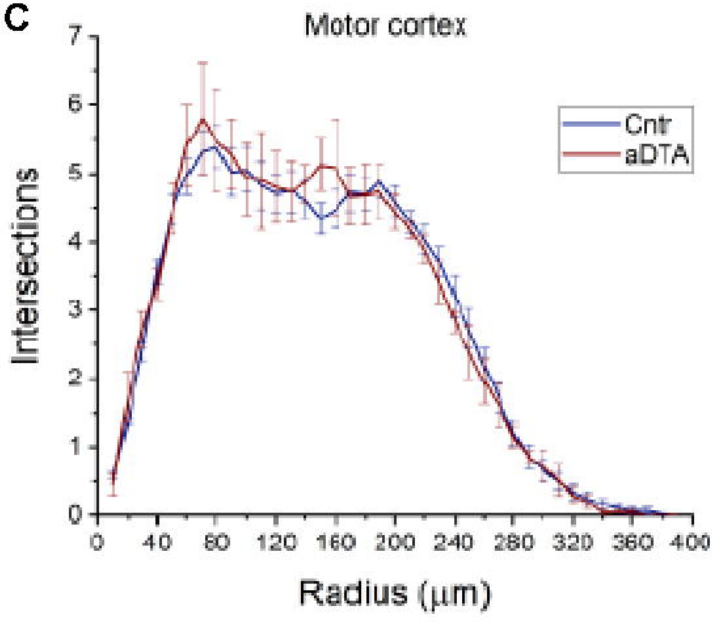
C
Motor cortex
Cntr
aDTA
Intersections
Radius (μm)
0
1
2
3
4
5
6
7
0
40
80
120
160
200
240
280
320
360
400

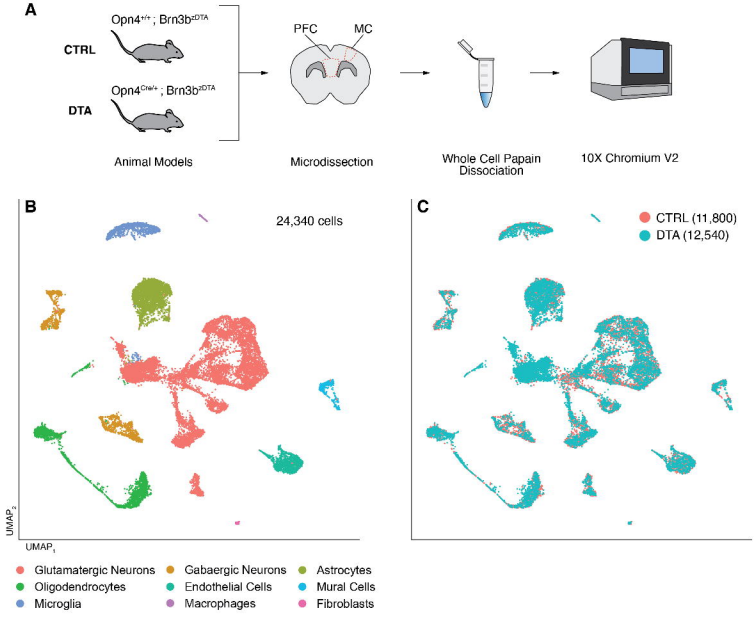
A
CTRL
Opn4+/+ ; Brn3bcDTA
DTA
Opn4Cre/+ ; Brn3bcDTA
PFC
MC
Animal Models
Microdissection
Whole Cell Papain Dissociation
10X Chromium V2
B
24,340 cells
UMAP2
UMAP1
C
CTRL (11,800)
DTA (12,540)
Glutamatergic Neurons
Gabaergic Neurons
Astrocytes
Oligodendrocytes
Endothelial Cells
Mural Cells
Microglia
Macrophages
Fibroblasts

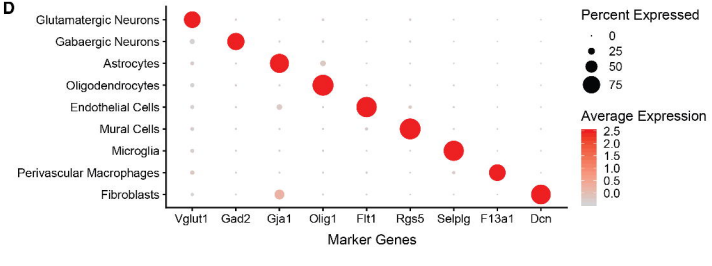
D
Glutamatergic Neurons
Gabaergic Neurons
Astrocytes
Oligodendrocytes
Endothelial Cells
Mural Cells
Microglia
Perivascular Macrophages
Fibroblasts
Vglut1
Gad2
Gja1
Olig1
Flt1
Rgs5
Selplg
F13a1
Dcn
Marker Genes
Percent Expressed
0
25
50
75
Average Expression
2.5
2.0
1.5
1.0
0.5
0.0

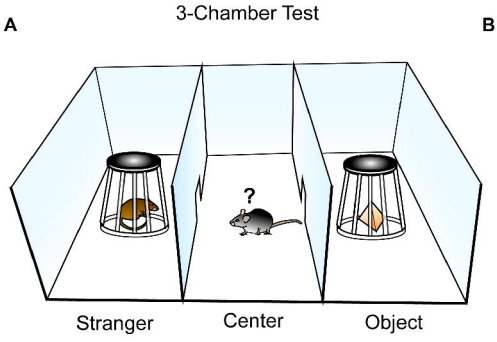
A
3-Chamber Test
?
Stranger
Center
Object

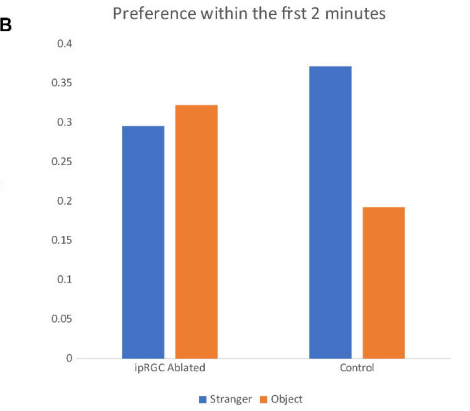
B
Preference within the first 2 minutes
0.4
0.35
0.3
0.25
0.2
0.15
0.1
0.05
0
ipRGC Ablated
Control
Stranger
Object

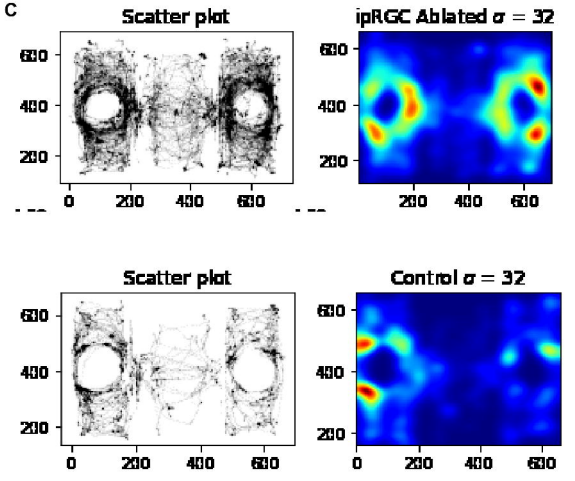
C
Scatter plot
ipRGC Ablated σ = 32
Scatter plot
Control σ = 32
600
400
200
0
200
400
600

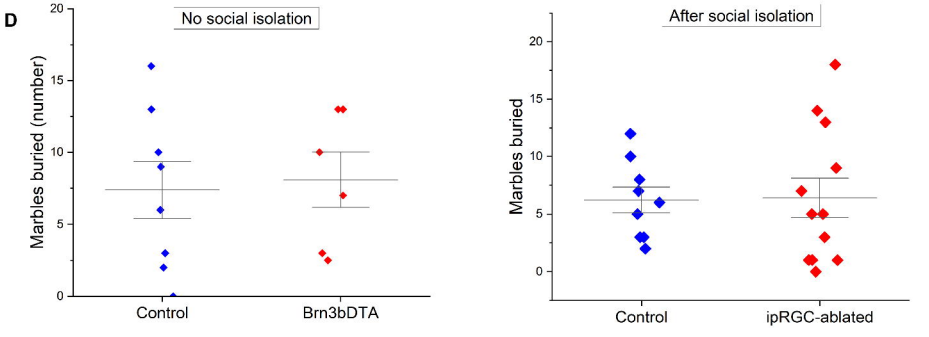
D
No social isolation
Marbles buried (number)
20
15
10
5
0
Control
Brn3bDTA
After social isolation
Marbles buried
20
15
10
5
0
Control
ipRGC-ablated

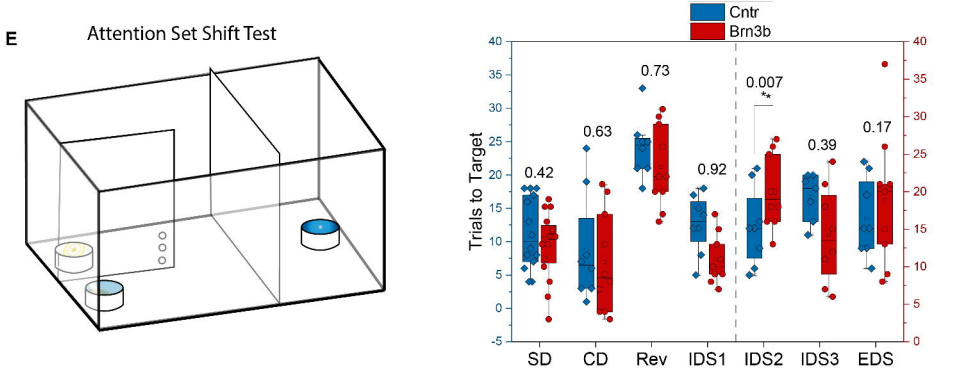
E
Attention Set Shift Test
Cntr
Brn3b
Trials to Target
40
35
30
25
20
15
10
5
0
-5
0.42
0.63
0.73
0.92
0.007
**
0.39
0.17
SD
CD
Rev
IDS1
IDS2
IDS3
EDS

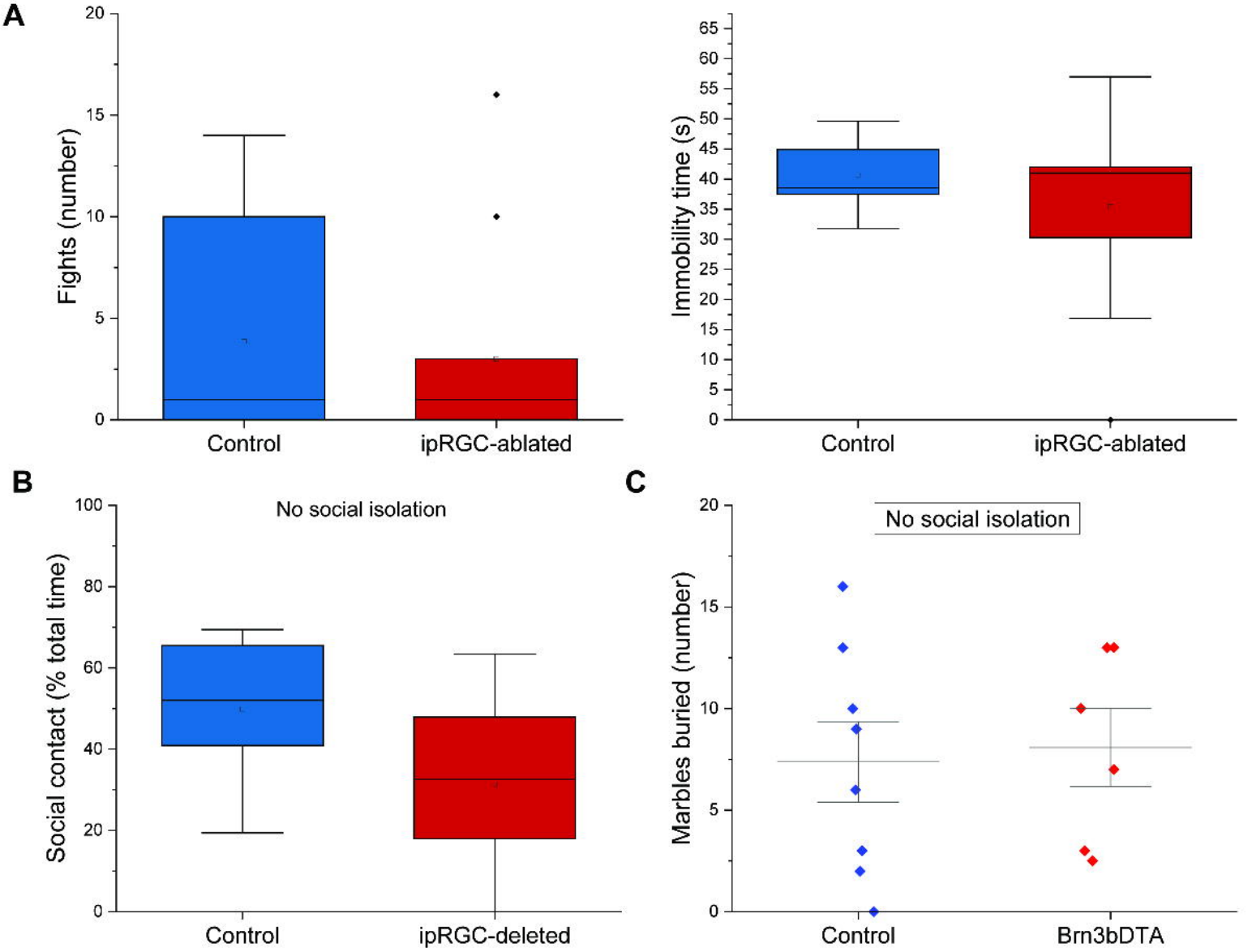
A
Fights (number)
Control
ipRGC-ablated
Immobility time (s)
Control
ipRGC-ablated
B
No social isolation
Social contact (% total time)
Control
ipRGC-deleted
C
No social isolation
Marbles buried (number)
Control
Brn3bDTA

D

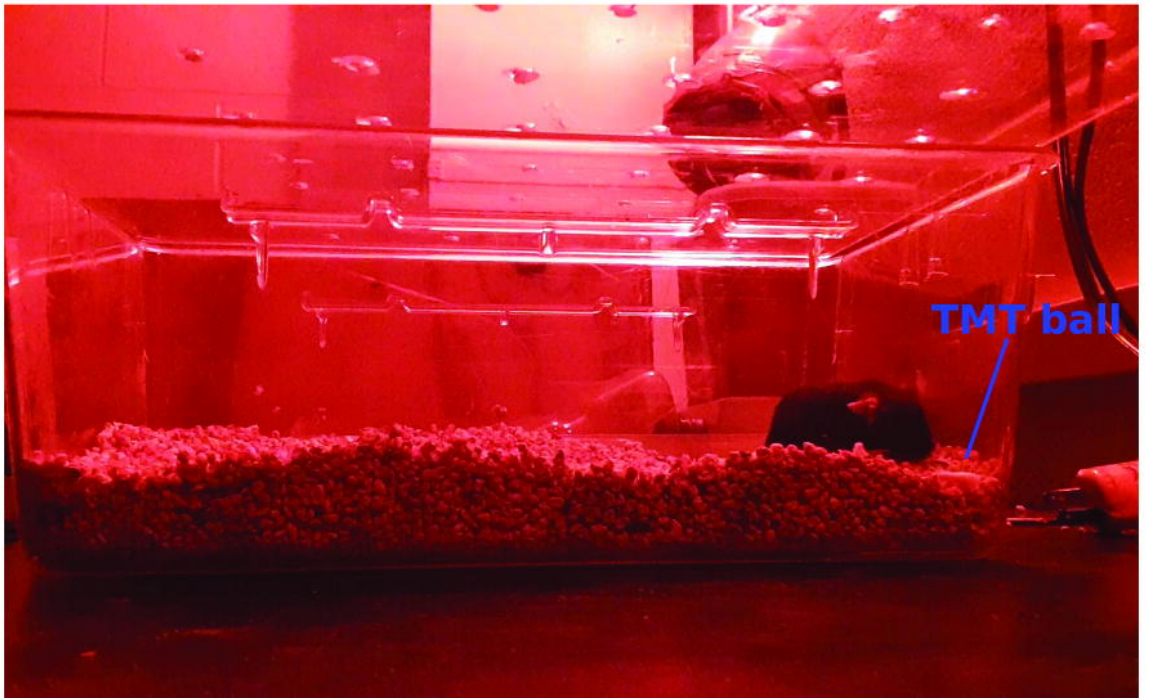
TMT ball

A

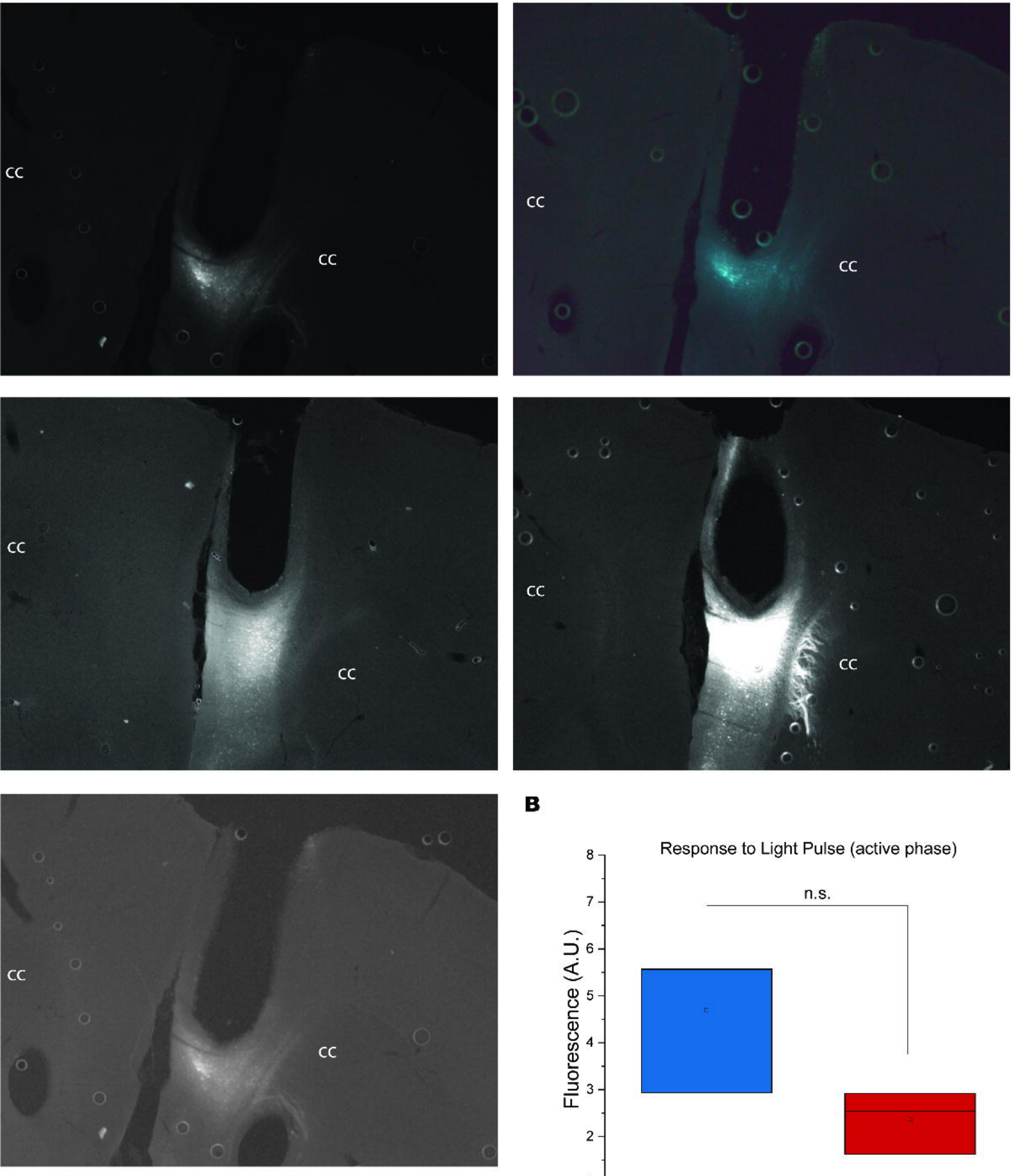
cc
cc
cc
cc
cc
cc
cc
cc
cc
cc

B

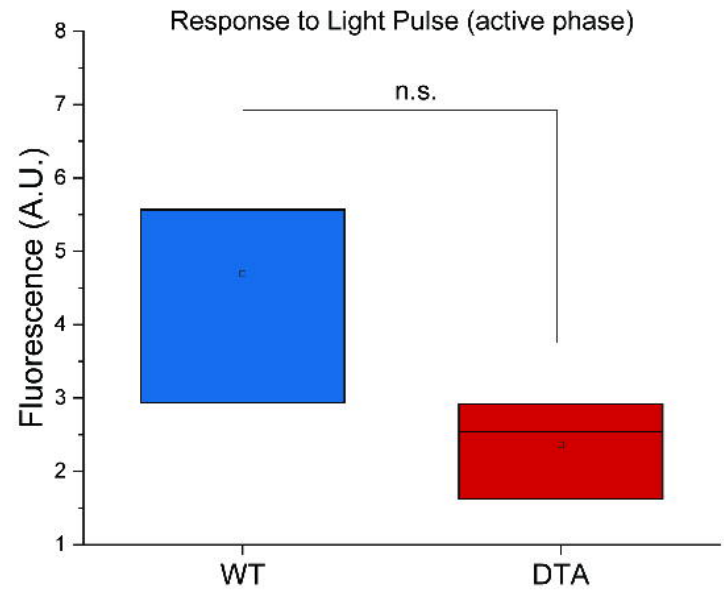
Response to Light Pulse (active phase)
n.s.
Fluorescence (A.U.)
8
7
6
5
4
3
2
1
WT
DTA

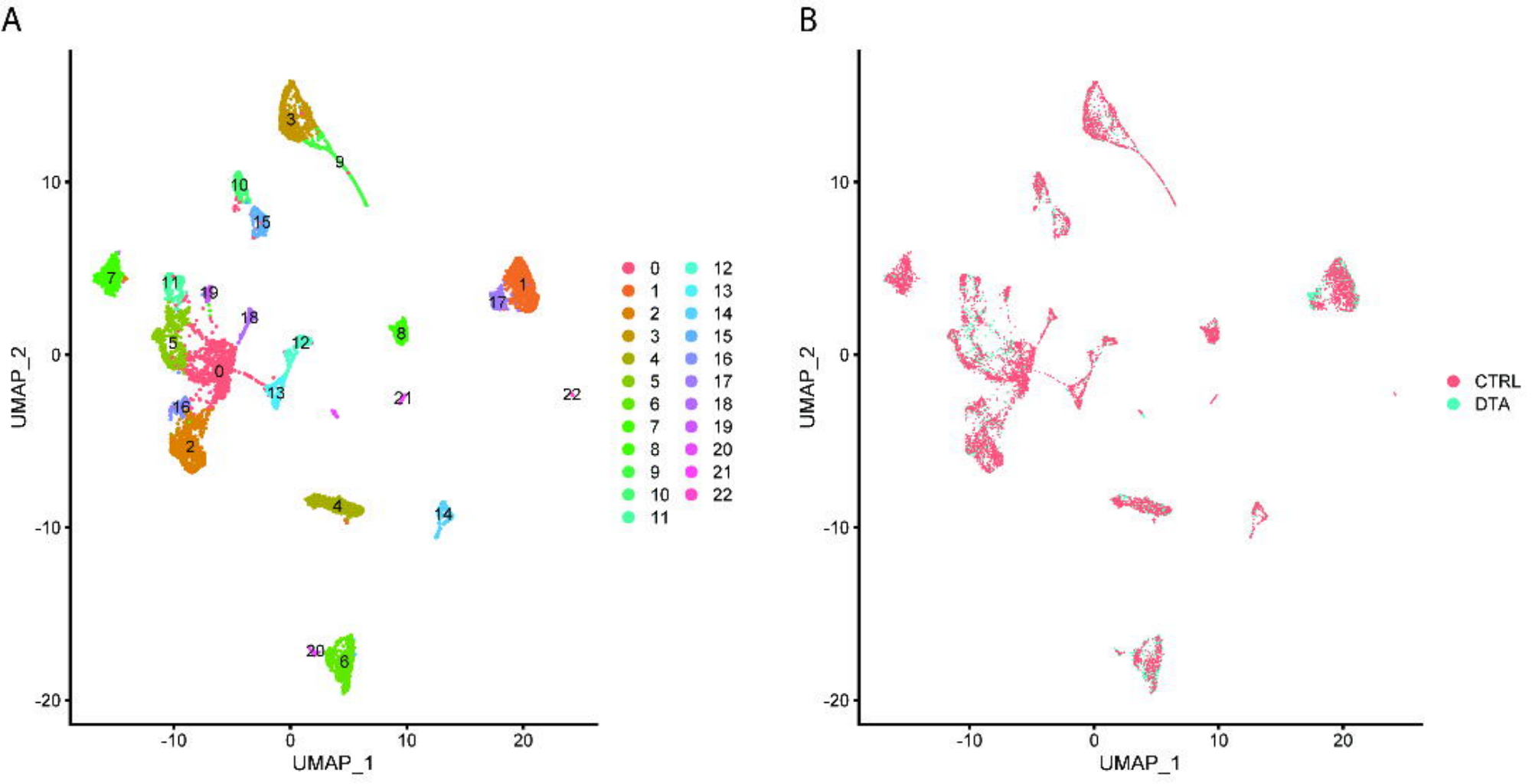
A
B
UMAP_1
UMAP_2
10
0
-10
-20
20
0
1
2
3
4
5
6
7
8
9
10
11
12
13
14
15
16
17
18
19
20
21
22
CTRL
DTA

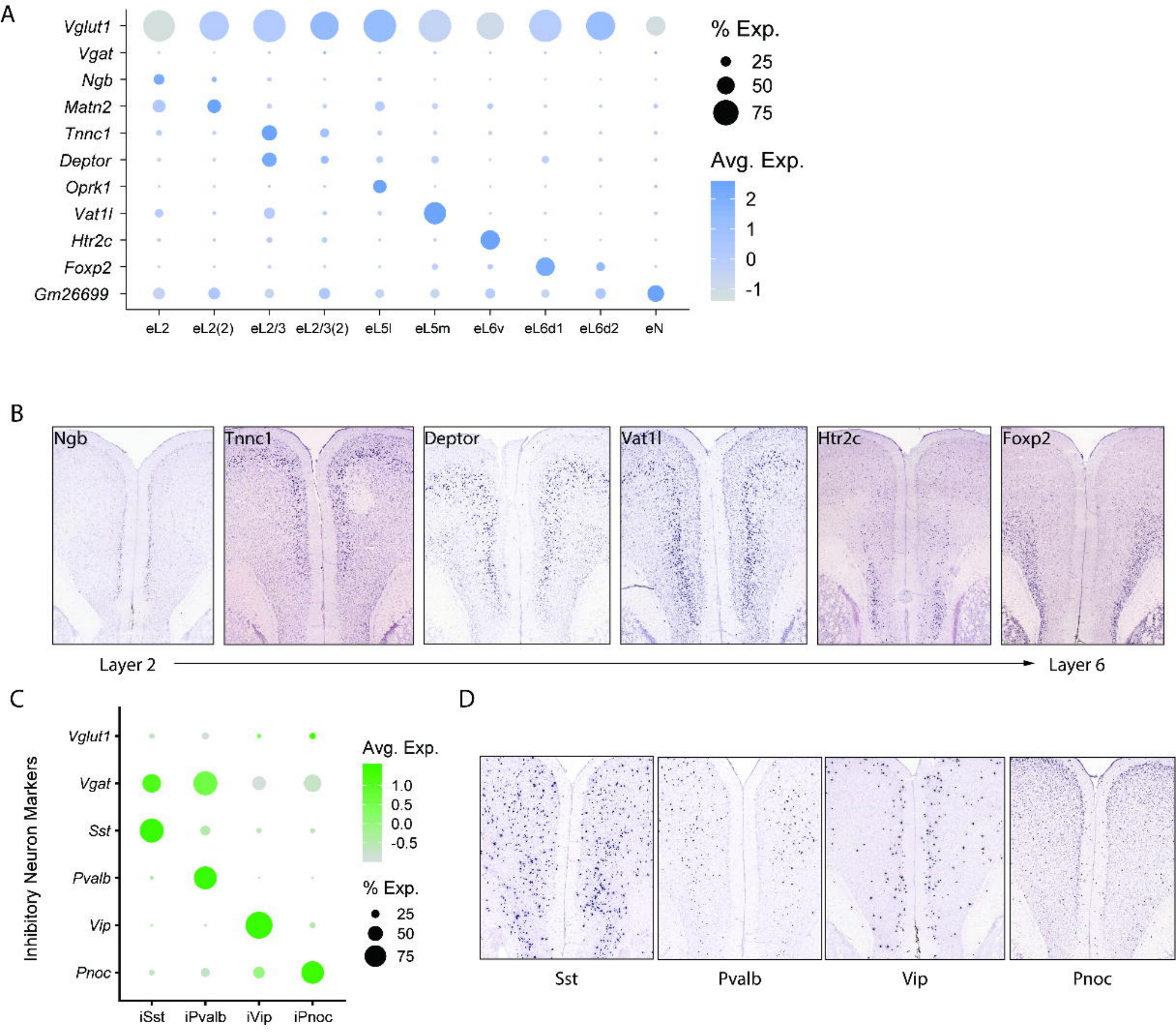
A
Vglut1
Vgat
Ngb
Matn2
Tnnc1
Deptor
Oprk1
Vat1l
Htr2c
Foxp2
Gm26699
eL2
eL2(2)
eL2/3
eL2/3(2)
eL5l
eL5m
eL6v
eL6d1
eL6d2
eN
% Exp.
25
50
75
Avg. Exp.
2
1
0
-1
B
Ngb
Tnnc1
Deptor
Vat1l
Htr2c
Foxp2
Layer 2
Layer 6
C
Inhibitory Neuron Markers
Vglut1
Vgat
Sst
Pvalb
Vip
Pnoc
iSst
iPvalb
iVip
iPnoc
Avg. Exp.
1.0
0.5
0.0
-0.5
% Exp.
25
50
75
D
Sst
Pvalb
Vip
Pnoc